



**HAL**  
open science

## Interconnect-Free Multibit Arithmetic and Logic Unit in a Single Reconfigurable $3 \mu\text{m}^2$ Plasmonic Cavity

Upkar Kumar, Aurelien Cuche, Christian Girard, Sviatlana Viarbitskaya, Florian Dell'Ova, Raminfar Al Rafrain, Gérard Colas Des Francs, Sreenath Bolisetty, Raffaele Mezzenga, Alexandre Bouhelier, et al.

### ► To cite this version:

Upkar Kumar, Aurelien Cuche, Christian Girard, Sviatlana Viarbitskaya, Florian Dell'Ova, et al.. Interconnect-Free Multibit Arithmetic and Logic Unit in a Single Reconfigurable  $3 \mu\text{m}^2$  Plasmonic Cavity. ACS Nano, 2021, 15 (8), pp.13351. 10.1021/acsnano.1c03196 . hal-02330410v2

**HAL Id: hal-02330410**

**<https://hal.science/hal-02330410v2>**

Submitted on 16 Aug 2021

**HAL** is a multi-disciplinary open access archive for the deposit and dissemination of scientific research documents, whether they are published or not. The documents may come from teaching and research institutions in France or abroad, or from public or private research centers.

L'archive ouverte pluridisciplinaire **HAL**, est destinée au dépôt et à la diffusion de documents scientifiques de niveau recherche, publiés ou non, émanant des établissements d'enseignement et de recherche français ou étrangers, des laboratoires publics ou privés.

# Interconnect-Free Multi-Bit Arithmetic and Logic Unit in a Single Reconfigurable 3- $\mu\text{m}^2$ Plasmonic Cavity

*Upkar Kumar<sup>1</sup>, Aurélien Cuche<sup>1</sup>, Christian Girard<sup>1</sup>, Sviatlana Viarbitskaya<sup>2</sup>, Florian Dell'Ova<sup>1,2</sup>, Raminfar Al Rafrain<sup>2</sup>, Gérard Colas des Francs<sup>2</sup>, Sreenath Bolisetty<sup>3</sup>, Raffaele Mezzenga<sup>3</sup>, Alexandre Bouhelier<sup>2</sup>, and Erik Dujardin<sup>1</sup>\**

<sup>1</sup>CEMES CNRS UPR 8011 and University of Toulouse, 29 rue J. Marvig, 31055 Toulouse, France.

<sup>2</sup>Laboratoire Interdisciplinaire Carnot de Bourgogne, CNRS UMR 6303, Université de Bourgogne Franche-Comté, 9 Av. A. Savary, 21000 Dijon, France.

<sup>3</sup>ETH Zurich, Department of Health Sciences and Technology, Schmelzberg-strasse 9, CH-8092 Zurich, Switzerland.

## ABSTRACT

Processing information with conventional integrated circuits remains beset by the interconnect bottleneck: circuits made of smaller active devices need longer and narrower interconnects, which have become the prime source of power dissipation and clock rate saturation. Optical inter-chip communication provides a fast and energy-saving option that still misses a generic on-chip optical information processing by interconnect-free and reconfigurable Boolean arithmetic logic units (ALU). Considering metal plasmons as a platform with dual optical and electronic compatibilities, we forge interconnect-free, ultracompact plasmonic Boolean logic gates and reconfigure them, at will, into computing ALU without any redesign nor cascaded circuitry. We tailor the plasmon mode landscape of a single  $2.6\text{-}\mu\text{m}^2$  planar gold cavity and demonstrate the operation and facile reconfiguration of all 2-input logic gates. The potential for higher complexity of the same logic unit is shown by a multi-input excitation and a phase control to realize an arithmetic 2-bit adder.

**Keywords:** logic gates, half-adder, reconfigurable device, plasmonics, cavity modes, non-linear photoluminescence

The significant energy dissipation and clock rate saturation faced by the microelectronics technology and the data-intensive applications originate in the interconnect bottleneck rather than in the elementary device performances.<sup>1-3</sup> Indeed, circuits made of smaller active devices need longer and narrower interconnects. An all-optical trafficking might be seen as a performing solution,<sup>4</sup> yet an optical transistor as energy frugal as current CMOS transistors would have to be reliably operated with less than one hundred photons,<sup>5</sup> which is a tremendous challenge.

One proposed paradigm shift consists in expanding the Boolean capabilities of the elementary unit beyond binary logic to reduce the need for interconnects. Promising candidates include solid-state qubits,<sup>6, 7</sup> elementary nanophotonics devices designed for photon manipulations<sup>4, 8-12</sup> and artificial neurons.<sup>13, 14</sup> However, irrespective of the specific assets inherent to the electronic, magnetic or optical nature of the implemented quantity, these elementary units have to be cascaded into quantum architectures, photonic circuits or neuromorphic networks to reach a full computing technology. They ultimately share the intrinsic topological and physical impediments of any interconnect-based technology. The topological limitation is globally assessed by the empirical Rent's rule that relates the number of elementary units per device to the number of input/output interconnect terminals required to fully exploit the computing power of the device.<sup>15-17</sup> The deviation from Rent's rule already observed in CMOS technology indicates the sub-optimal usage of the available computing power when the device cannot accommodate enough interconnects.<sup>15</sup> Further physical limitations of interconnected circuits, for which only partial solutions are foreseen, include logic-level restoration, decoherence and error compensation, bandwidth limitation, (de)multiplexing network integration and downsizing.<sup>5, 18, 19</sup>

Conversely, a radically different concept aims at condensing a full Boolean computing function in a self-sufficient standalone and interconnect-free device. Only few hardware

solutions to this concept have been developed from single molecules,<sup>20-22</sup> electromechanical resonators<sup>23, 24</sup> and microwave metamaterials.<sup>25, 26</sup> Despite their technical differences, they jointly contribute to the unconventional implementations of complex mathematical or logic computation without relying on cascaded elementary units and thus obviate the constraints of Rent's rule.

The main challenge for these approaches is then shifted towards the inverse design of the adequate structure to perform a targeted logical or arithmetic operation. For example, centimeter-scale microwave metastructures were successfully inverse designed by deep learning methods to perform a particular complex mathematical operation.<sup>25-28</sup> Unfortunately, even these solutions suffer from one or several intrinsic limitations such as very low bandwidth, operation at cryogenic temperature and in ultrahigh vacuum, uncompetitive miniaturization and/or significant energy dissipation. In this regard, a photonic approach of this integrative paradigm would provide a high bandwidth, energy-frugal technology at room temperature.

Here, we propose a holistic implementation of standalone and all-optical devices performing reconfigurable universal Boolean logics and arithmetic at visible frequencies. In order to obviate the diffraction limitation of photonic devices and to maximize the device compactness while restraining minimal loss, our devices exploit plasmon excitations in single-crystal gold structures.<sup>8, 12, 29</sup> A plasmon mode landscape<sup>30</sup> is tailored in a two-dimensional (2D) metallic structure with micrometric footprint to implement logic gates that are reconfigured, at will, into more complex computing arithmetic and logic units (ALU) without requiring any redesign or cascaded circuitry. In particular, we experimentally demonstrate the operation and facile reconfiguration of all possible 2-input, 1-output logic gates in a single planar multimodal plasmonic cavity. The potential for higher Boolean complexity, without compromising the high compactness, is demonstrated first by operating our device as several ASIC-like Boolean functions (ASIC: application-specific integrated circuits) from a 3-input excitation and finally

by showing that controlling the relative phase between multiple excitation beams makes it possible to realize the first 2-bit adder in the same ALU.

## Results and Discussion

The general principle of plasmonic modal logic gate is illustrated in Fig. 1A. Surface plasmons (SP) sustained by an ultrathin crystalline gold microplatelet are confined in a two dimensional fused double hexagon shape that creates resonant SP modes. The resulting near-field patterns are distributed over the entire structure as a set of strongly contrasted localized and enhanced spots.<sup>31</sup> The large number of sustained modes is fully described by the SP local density of states (SPLDOS) that is defined as the number of plasmonic modes per unit energy and elementary volume at any location inside the metal (See details and maps in Fig. S2 in Supporting Information, SI) in a similar way that electromagnetic (or photonic) LDOS applies to electromagnetic modes that are defined outside the metal.<sup>31</sup> The design of the device is based on our early gedanken proposal of NAND and COPY gates implementation in a dimer of quasi-hexagonal Au prisms.<sup>31</sup> To promote an optimal input-output information transfer,<sup>32, 33</sup> we focus here on a continuous double hexagonal shape (Figs. 1B, 1C) with a size adjusted to show transmittance resonances in the visible (720 nm) to near IR (810 nm) region as shown in Figure S3D.<sup>33</sup> Our devices are fabricated by focused ion beam (FIB) milling single crystalline gold microplatelets produced in solution and drop-casted onto ITO-coated glass coverslips.<sup>33</sup> The ion dose is adjusted to minimize the substrate etching and gold amorphization. Any peripheral Au regions as seen in Figure 1C are removed by FIB to leave a standalone double hexagon with sharp edges and preserved crystallinity displayed in Figure S2A.<sup>34</sup> The area of the structure is  $2.65 \mu\text{m}^2$  (extremal size of  $2.5 \times 1.1 \mu\text{m}$ ).

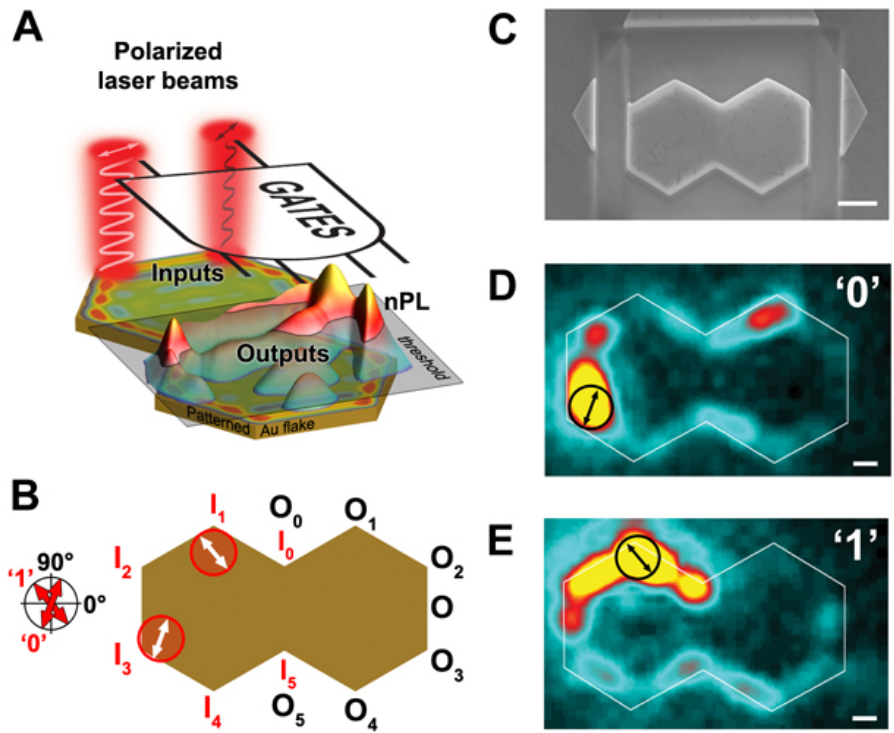


**Figure 1.** Principle, fabrication and addressing of reconfigurable plasmonic modal logic gates. (A) Schematic of a 2D crystalline gold cavity shaped into a double hexagon device (brown) that bears plasmonic eigenstates contributing to the in-plane SPLDOS shown as a watermarked map. Two laser beams, with specific linear polarizations that encode the Boolean '0' and '1' inputs (see inset), excite sequentially the device that produces a remote non-linear photoluminescence (nPL) signal with strong spatial variations in the output region. A nPL signal exceeding a threshold value corresponds to a Boolean '1' gate output. (B) Locations of the inputs  $I_1$  to  $I_4$  and output  $O_1$  to  $O_4$  considered in this work. Positions 0 and 5 are considered as either input or output depending on the operating configuration. A two-beam excitation is exemplified for inputs  $I_1$  and  $I_3$  with input polarizations  $130^\circ$  (Boolean '1') and  $70^\circ$  (Boolean '0') respectively. (C) SEM image of a logic gate device being milled by FIB in a single crystalline Au microplate. The peripheral Au regions are milled away before optical experiments. (D) Wide-field nPL images obtained by exciting the structure in position  $I_3$  with linearly polarized light oriented at  $70^\circ$  from the device long axis. The map, recorded in arbitrary units on an 8-bit registry, constitutes the response function of the device to a Boolean '0' in input  $I_3$ . (E) Similar nPL map providing the response function of the device to a Boolean '1' (polarization oriented at  $130^\circ$ ) in input  $I_1$ . Scale bars are (C) 500 nm, (D, E) 200 nm.

When a femtosecond pulsed laser is focused on a high SPLDOS spot, it efficiently drives the plasmon resonance and generates non-linear photoluminescence (nPL) not only at the excitation spot, but also in the most remote regions of a specific near-field pattern.<sup>31, 35, 36</sup> In this work, the nPL is used as an all-optical observable of the transfer function of the device.<sup>33</sup> The threshold readout of the nPL signal intensity, recorded in arbitrary units on a 8-bit registry from a

diffraction limited region, represents the logical output of the device that is associated to the logical inputs encoded in the linear polarization directions of the excitation beams. When the nPL signal is collected in confocal mode as displayed in Figures S1A and S2, it directly reveals the squared SPLDOS pattern<sup>31</sup> that shows a marked enhancement distributed along the perimeter of the structure.

In particular, spots localized at the ten vertices exhibit a high nPL intensity or, equivalently, a large SPLDOS, which are used hereafter as input ( $I_n$ ) or output ( $O_n$ ) ports (Fig. 1B). In order to operate the device, a linearly polarized pulsed laser focal spot ( $\lambda = 810$  nm) is now parked in one of the inputs and the nPL signal distributed over the entire structure is collected in wide-field microscopy as described in Fig. S1B. Figs. 1D and 1E show the wide-field images recorded for inputs  $I_3$  and  $I_1$  and polarizations  $70^\circ$  and  $130^\circ$  respectively. Besides the strong local response from the impinging site, nPL is essentially emitted along the perimeter with an intensity pattern that varies markedly upon changing the excitation point or the excitation polarization.

We assign a Boolean value of '0' (resp. '1') to the excitation polarizations  $70^\circ$  (resp.  $130^\circ$ ) and construct the response map of the gate device in the 0-1 input configuration by summing the intensity images 1D and 1E. This non-coherent response results from the sequential nPL transmittance from the first and second input. It is equivalently obtained by the digital sum of the two independent intensity images or by the cumulative recording of the intensity produced by the excitation of both inputs, provided that the impinging pulses are well separated in the time domain (Figs. S1 and S4). By recording the two extra nPL wide-field images with  $I_1$  (resp.  $I_3$ ) excited with a  $70^\circ$ -polarized (resp.  $130^\circ$  polarized) beam, we can complete the functional response of the device with the four 2-input configurations (0-0, 0-1, 1-0 and 1-1) as displayed in Figures 2A-E. The marked differences between the four response maps observed over the entire structure affect all the vertices of the rightmost hexagon which can each accommodate

one output port. In Figure 2F, the intensity profiles of the four configurations are plotted in arbitrary units along the dotted perimeter in Figure 2A. For a readout threshold of 20, four different gates are simultaneously realized in the five outputs: NOT  $I_1$  in  $O_1$ , COPY  $I_1$  in  $O_2$  and  $O_4$ , AND in  $O_3$  and Tautology in  $O_5$  (Fig. 2G). If we consider the output port  $O_3$  and simply change the readout threshold to 7.5, the AND gate is reconfigured into an OR gate (Fig. 2H) and further into a Contradiction gate by raising the threshold to 60, for example (Fig. 2I).

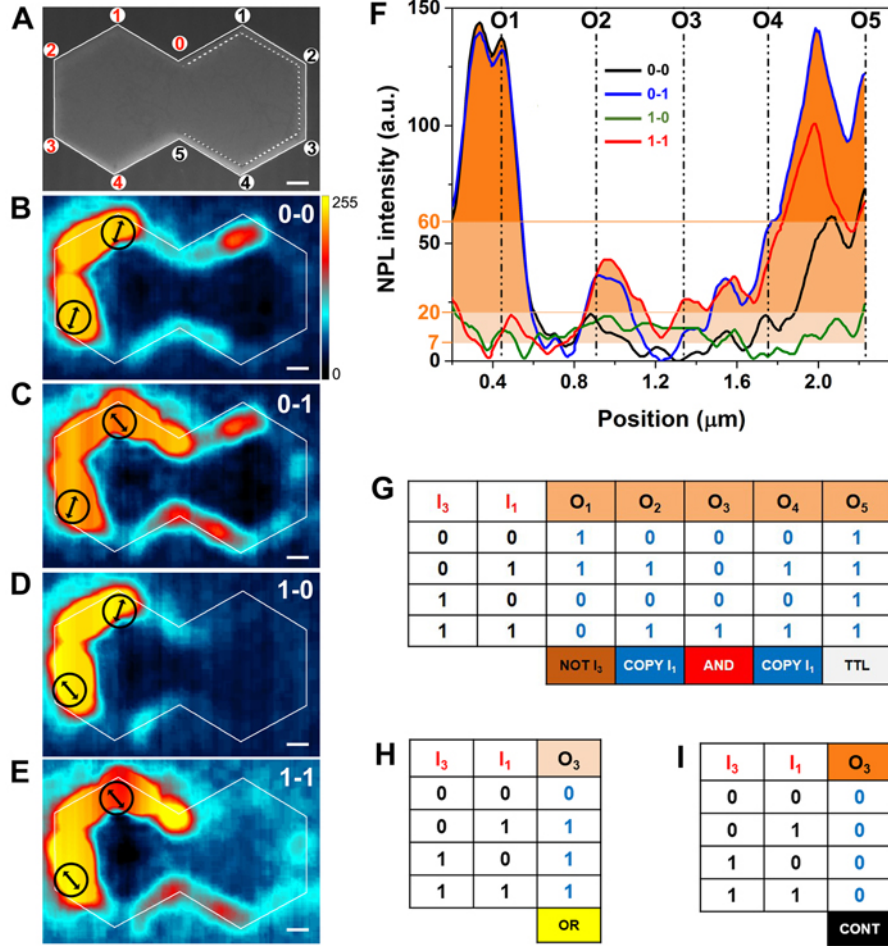


**Figure 2.** Multiple 2-inputs 1-output logic gates using the remote non-linear response of plasmonic eigenstates in a single double hexagonal gold cavity. **(A)** SEM image of the double hexagonal cavity milled from a 20-nm thick Au nanocrystal. The overall device area is smaller than  $3.0 \mu\text{m}^2$ . Scale bar is 200 nm. **(B-E)** Non-linear photoluminescence transmittance maps constructed by the summation of wide field images obtained for fixed excitation in inputs  $I_3$  and  $I_1$  with a linearly polarized focused laser beam (FWHM 300 nm) as indicated by the black circles and arrows. Polarization direction at  $70^\circ$  (resp.  $130^\circ$ ) is assigned to a Boolean input "0" (resp. "1"). The four maps correspond to the four possible input configurations: **(B)**  $I_1$  and  $I_3$  are "0"; **(C)**  $I_3$  is "0",  $I_1$  is "1"; **(D)**  $I_3$  is "1",  $I_1$  is "0"; **(E)**  $I_3$  and  $I_1$  are "1". The common color scale is given next to (B). Scale bars are 200 nm. **(F)** Non-linear photoluminescence intensity profiles from the maps in **(B-E)** along the same dotted line shown in **(A)**. Three readout thresholds (7.5, 20, 60) are indicated in three shades of orange. The centers of the output locations ( $O_1$  to  $O_5$ ) are indicated by the vertical dash-dot-dot lines. When the nPL signal exceeds the threshold in one output location, it is assigned to a Boolean output "1". **(G)** Combined truth tables for all five output positions read at threshold 20. Depending on the readout location, the devices perform simultaneously AND, NOT( $I_3$ ), COPY( $I_1$ ) and Tautology gates. **(H, I)** Upon lowering the threshold to 7.5 or raising to 60, the output  $O_3$  is instantaneously reconfigured from a AND into a OR gate **(H)** and then a Contradiction gate **(I)**.

Besides choosing the output location or the readout threshold, other tunable parameters can be used to achieve multiple instantaneous reconfigurations of the function of the same device and extend the list of 2-input gates implemented (Figure 3). First, we change the set of polarizations encoding the Boolean inputs. If we use  $110^\circ$  and  $150^\circ$  instead of  $70^\circ$  and  $130^\circ$ , the output  $O_1$ , is changed from an inverter (NOT) to a NAND gate at threshold 45 (Figs. 3A, 3B). The complete set for this excitation scheme is shown in Figure S5. Alternatively, if we input the information in two other locations,  $I_0$  and  $I_2$ , with  $90^\circ$  and  $10^\circ$  encoding '0' and '1' inputs as shown in Figures 3C and 3D (see details in Fig. S6), the farthest outputs  $O_2$  and  $O_4$  provide the simultaneous negation of both inputs at the same threshold 30 while only one NOT gate was obtained in Figure 2. Inverting the input polarizations, *i.e.*  $10^\circ$  and  $90^\circ$  encode '1' and '0' respectively, converts the  $(O_4, O_2)$  output pair into SWAP( $I_0, I_2$ ), which is a more complex 2-input, 2-output gate. When we tune the excitation wavelength to 750 nm instead of 810 nm, we recruit a different set of eigenmodes and, once again, reconfigure the logic function. For example, Figures 3E and 3F, show the nPL signal collected when exciting inputs  $I_0$  and  $I_3$  at 750 nm with polarization  $100^\circ$  ('1' input) and  $20^\circ$  ('0' input) resulting in a NOR gate in outputs  $O_2$  and  $O_4$  at threshold 130 (see details in Fig. S6).

The set of ten different and reconfigurable 2-bit logic gates demonstrated experimentally in Figures 2 and 3 includes universal gates (NAND, NOR) or the (AND, OR, NOT) set that could, in principle, be concatenated to implement any Boolean logic function. However, this classical approach<sup>8, 12</sup> requires the efficient transfer of the output signal of one gate to the next one, which would exponentially increase the size of the required waveguide network connecting the gates as Boolean complexity rises. More importantly, this approach would assume a gain mechanism to compensate for the intrinsic dissipation of the information signal carried from one universal gate to the next through the plasmonic circuitry.

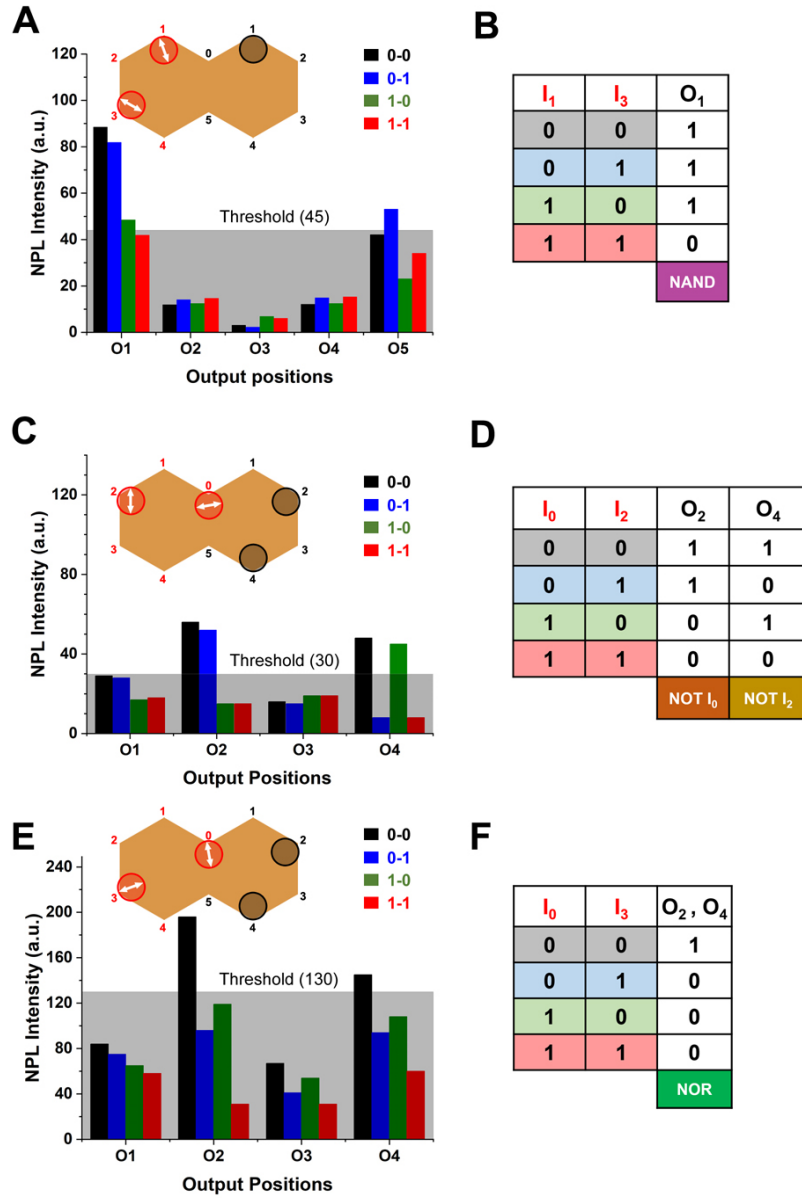


**Fig. 3.** Multiple ways to reconfigure the same logic device to get all possible gates. **(A, B)** Choosing the polarization direction encoding the Boolean inputs. **(A)** When the  $70^\circ$  and  $130^\circ$  choice for "0" and "1" in Fig. 2 is replaced by  $110^\circ$  and  $150^\circ$ , the device response is modified as summarized by the histograms. **(B)** At threshold 42, output  $O_1$  is reconfigured from a NOT to a universal NAND gate. **(C, D)** Choosing the input locations. **(C)** Histogram summary of the device response when inputs  $I_0$  and  $I_2$  are selected with polarizations  $10^\circ$  ("0") and  $90^\circ$  ("1"). **(D)** At the same threshold 30,  $O_2$  and  $O_4$  are reconfigured to NOT( $I_0$ ) and NOT( $I_2$ ) respectively. **(E, F)** Choosing the excitation wavelength. **(E)** Histograms of the device response in  $O_1$  to  $O_4$  upon excitation at 750 nm in inputs  $I_0$  and  $I_3$  with polarizations  $20^\circ$  ("0") and  $100^\circ$  ("1"). At threshold 130, universal NOR gates are performed in  $O_2$  and  $O_4$ . **(F)** Table of truth of the NOR gate in  $O_2$  and  $O_4$ .

Instead, our modal logic gates obviate these two impediments of classical circuit architectures by exciting the relevant sub-set of SP modes able to directly realize a complex Boolean

function. This is illustrated in Figure S7 where three inputs ( $I_1$ ,  $I_3$  and  $I_4$ ) are now excited with the same set of polarizations ( $70^\circ$  and  $130^\circ$ ) as in Figure 2. Without any parametric optimization or adjustment nor redesign of the cavity shape, the direct Boolean response of the double hexagon device, in  $O_1$  and  $O_4$  for example, realizes a 3-bit OR, a 3-bit AND and other combinations of 3-input OR and AND gates such as  $(\overline{I_1} \text{ AND } I_4) \text{ OR } I_3$ .

Importantly, this shows that our approach accommodates higher gate complexity in standalone devices without cascading the elementary functions shown in Figure 2 and 3. Before expanding our approach towards ASIC-like logic devices, an optimization step will be necessary in order to maximize the global signal level but also the Boolean contrast, i. e. the intensity difference between the lowermost analog signal corresponding to a "1" output and the highest signal assigned to a "0" output. The large number of design and operating parameters exploited here to establish the proof-of-concept of reconfigurable modal gate implementation suggests that such an optimization is a challenge *per se*. It could be carried out, for instance, using photonic inverse design<sup>27</sup> or evolutionary<sup>37, 38</sup> algorithms that have successfully solved complex optimization questions such as the directivity and selectivity of nano-optical antenna or multi-signal plasmonic transmission networks.

Next, we demonstrate that the modal gate design is not restricted to pure Boolean logic gates and functions but can also perform arithmetic operations such as the modulo 2 additive gates, XOR and NXOR, and the half-adder unit that adds two numbers to produce a sum and a carry.

So far, in our simple additive experimental scheme, the gate output results from the accumulation of the nPL signal generated by the sequential excitation of the first and second inputs. Consequently, if the output is sub-threshold for the (0-0) configuration and supra-threshold for both (0-1) and (1-0) configurations, it will be even higher for the (1-1) excitation, therefore preventing the implementation of the (N)XOR gates.

However, if we consider a temporal overlap of the exciting pulses impinging on both inputs, the resulting coherent plasmon mode excitation can be tuned by varying the relative phase between the incoming pulses.<sup>39</sup> In particular, we can select a phase difference that produces destructive SP interferences at the output ports in the (1-1) configuration. In such a scheme, a lower output signal is achieved for (0-0) and (1-1) compared to both responses of (0-1) and (1-0) making it possible to encode arithmetic Boolean functions. To explore such operating conditions of the structure, we have modified our Green's Dyadic Method (GDM) transmittance numerical tool<sup>33</sup> and implemented multiple simultaneous Gaussian beam excitations whereby several input ports can be chosen, each with a defined phase of the impinging electromagnetic field (See SI for details).

Figures 4A-D show the computed coherent near-field response of the double hexagon when two in-phase beams ( $\Delta\varphi = \varphi_2 - \varphi_0 = 0^\circ$ ) are focused on inputs  $I_0$  and  $I_2$ , their polarization directions being either  $110^\circ$  or  $150^\circ$ . A contrasted distribution of the transmitted nearfield is produced that reaches the remote right side of the structure where the local field intensity is modulated by the change in the incident polarization configuration. Tuning the phase shift  $\Delta\varphi$ , for example with a delay line and a spatial light modulator, produces a monotonous sweep of the near-field intensity across the entire double hexagon as illustrated in movie SM2. In specific locations, strong variations are observed, by about one order of magnitude of the field intensity, indicating significant output changes that can be exploited to implement coherent modal logic gates. This is illustrated by considering the two peripheral regions  $O_1$  and  $O$  (see Figs. 4E, H, K) delineated with black squares in Figures 4A-D. The in-phase ( $\Delta\varphi = 0^\circ$ ) output response from  $O_1$  follows an XOR table of truth with an output intensity for the (0-1) and (1-0) excitation configurations that exceeds significantly the one for the configurations (0-0) and (1-1) as shown in Figure 4G. When the two input lasers are dephased so that  $\Delta\varphi = 180^\circ$ , the same output port  $O_1$  is converted into a NXOR gate output, in the exact same excitation conditions (Figs. 4H-I).

Indeed, Figure 4J shows that the transmittance signal for the (0-0) and (1-1) excitations exceeds the value obtained for both (0-1) and (1-0) excitations. Interestingly, the overall near-field transmittance signal integrated over the  $220 \times 220$  nm red (resp. green) hatched zones in Fig. 4F (resp. 4I) reaches about 4-5% of the excitation field intensity,  $|E_0|^2$ , integrated over a similar diffraction limited area. These results strongly suggest that such a coherent response will be detectable experimentally, by nPL-based mapping, a method that enhances near-field transmittance contrast as shown in our recent work on modal routing devices.<sup>33</sup>

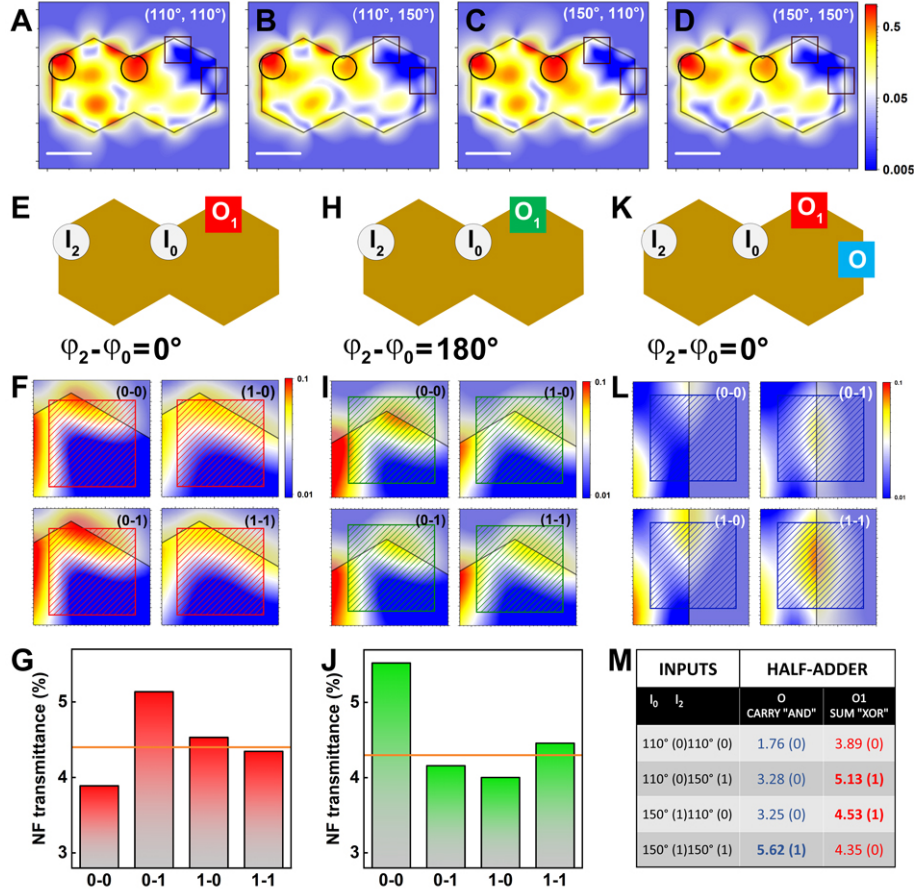


**Fig. 4.** Coherent excitation and phase tuning yield XOR, NXOR and 1/2-adder logic gates. (A-D) (0,0), (0,1), (1,0) and (1,1) near-field (NF) transmittance maps of the double hexagon device obtained with a simultaneous double excitation in  $I_0$  and  $I_2$  (black circles) with incident linear polarization  $110^\circ$  ("0") and  $150^\circ$  ("1") and excitation phases  $\varphi_2 = \varphi_0 = 0^\circ$ . Red squares indicate the outputs considered hereafter. Scale bars are 500 nm. (E-G) XOR gate realized in output  $O_1$  as sketched in (E) with  $\varphi_2 - \varphi_0 = 0^\circ$ . (F) Zoomed NF transmittance maps near  $O_1$  for the four logic input configurations. The  $220 \times 220$  nm red hatched square delineates the area used for numerical signal integration. (G) Histogram of the integrated NF transmittance values (see the red-hatched area in (F)) and normalized to a similar area of the exciting beam. The XOR gate is obtained for a threshold of 4.4%. (H-J) Sweeping  $\varphi_2 - \varphi_0$  to  $180^\circ$  provides an implementation of the NXOR gate in output  $O_1$  as sketched in (H). (I) Zoomed NF transmittance maps near  $O_1$  for the four logic input configurations. The  $220 \times 220$  nm green hatched square delineates the area used for numerical signal integration. (J) Histogram of the normalized integrated NF transmittance values (see the green-hatched area in (I)) The NXOR gate is obtained for a threshold of 4.3%. (K-M) Half-adder logic function obtained simultaneously by combining the XOR gate in  $O_1$  with an AND gate in O (blue square) with  $\varphi_2 - \varphi_0 = 0^\circ$  as sketched in (K). (L) Zoomed NF transmittance maps near O for the four logic input configurations. (M) Truth table of a half-adder logic device obtained by reading the normalized NF transmittance integrated over the red- and blue-hatched regions in (F) and (L) respectively. The Boolean values between parenthesis are defined with a common readout threshold of 4.4%.

With the (N)XOR gates, we complete the entire set of 2-input 1-output gates obtained by the Boolean reconfiguration of a single device. Since our modal plasmonic gate approach offers the possibility to read-out multiple outputs, we can now consider combining the XOR and the AND gates to implement the first simple arithmetic and logic computing unit (ALU), the half-adder.

In Figures 4K-M, we revert to in-phase ( $\Delta\phi = 0^\circ$ ) excitation of  $I_0$  and  $I_2$  and consider the extra output  $O$  located in the middle of the rightmost edge of the structure. The near-field transmittance maps in Figure 4L show a robust AND gate in  $O$  that can be combined with the XOR gate demonstrated in output  $O_1$ . When a common readout threshold of 4.4% is set on both outputs, a 2-bit adder, commonly named half-adder, with the sum and the carry is realized as detailed in the table of truth of Figure 4M. Importantly, the construction of the all-optical half-adder proposed here does not rely on the concatenation of the two AND and XOR sub-gates. Such a classical cascaded circuit would be seriously hampered by the intrinsic loss of plasmon-based devices. Instead, our approach consists in recruiting the adequate eigenmodes among the many sustained by the cavity to implement a more complex gate in the same reduced footprint, therefore both AND and XOR gates reach the same *ca.* 4% output level.

This illustrates that the design of the cavity determines the available eigenmodes, which are then selected by the illumination and read-out schemes, to achieve a targeted logic function. Since numerous modes coexist in our mesoscale structures, a very versatile reconfiguration is possible using wavelength, sets of polarization, input and output ports or threshold as function selectors. Our modal plasmonic gate approach can be extended beyond the 2-bit half-adder towards more complex  $n$ -bit Boolean ALU, that would ideally, but not solely, perform  $n$ -bit full adder (AND, XOR) and NOT functions. Our demonstrators show that this holistic ALU design does not require to cascade elementary units in proportion of the targeted functional complexity making it impervious to the detrimental effects of Joule losses pertaining even in crystalline

plasmonic devices. As in the case of purely logic complex functions (See Fig. S7 for details), the implementation of  $n$ -bit ALU combining Boolean and arithmetic functions will require a global parametric optimization for which photonic inverse design and evolutionary tools could be applied in order to maximize the output intensities and locations and the signal-to-noise ratio.<sup>27, 37, 38, 40</sup> Yet, akin the analogous computing based on metasurfaces,<sup>28</sup> the main challenge towards increased logic complexity resides in the inverse design of the adequate plasmonic cavity to reach a specific ALU function for which more advanced deep learning<sup>41-43</sup> approaches are foreseen to provide powerful tools.

## Conclusion

We have developed a holistic design of reconfigurable nano-optical logic devices based on the 2D patterning of single-crystalline metallic cavities. By creating a large set of specific plasmon eigenmodes that possess both localized features, used as input/output ports, and delocalized extension over the double hexagon cavity, we were able to realize and reconfigure, at will, all twelve possible 2-input, 1-output logic gates in a single flat plasmonic cavity. This principle was generalized by demonstrating complex 3-inputs Boolean functions in the same cavity without resorting to networking elementary gates. Finally, our approach provides a compact and cascade-free optical platform to arithmetic and logic functions as shown by driving the double hexagon as a 2-bit half-adder. Bringing the proof-of-concept of modal plasmonic gates and ALU demonstrated here into a future practical implementation will benefit from two recent advances. First, further Boolean generalization towards complex gates and ALU is a non-trivial task for which the latest inverse design tools can be advantageously applied.<sup>43, 44</sup> Second, progress in light source integration by embedding single photons sources,<sup>45-50</sup> or by tunnel current-driven emission,<sup>51-53</sup> will enable integrating our planar 2D Boolean devices with laser-free on-chip optical excitation and ultimately to plasmon-based quantum technologies.<sup>54</sup>

## Methods and Experimental

**Au microplate synthesis.** The crystalline gold microplatelets studied here are synthesized using  $\beta$ -lactoglobulin protein fibrils. Purified Beta-lactoglobulin protein monomer of 2 wt% is initially heat treated at 90°C and pH 2 condition for 5 hours resulting the formation of the multi-stranded amyloid fibrils. The microplatelets are prepared by mixing a 0.01M aqueous solution of H<sub>2</sub>AuCl<sub>4</sub> with 0.6 wt% solution of  $\beta$ -lactoglobulin fibrils. The solution is then heated at 55°C for 24 hours. The microplatelets are 20-40 nm in thickness and the typical in-plane dimensions are in the range of 1-15  $\mu$ m.

**FIB patterning of double hexagon cavities.** The double hexagon structures are fabricated by focused ion milling of hexagonal microplatelets with diameter of 3-5  $\mu$ m using a gallium ion beam on a Zeiss 1540 XB dual beam microscope interfaced with a Raith Elphy Multibeam pattern generator. To ensure minimal substrate milling while thoroughly etching the gold, typical ion current of 1.0 pA and dose of 8000  $\mu$ C.cm<sup>-2</sup> are used. The milling protocol consists in etching out the double hexagon pattern first with minimal beam rastering along the double hexagon edges. The peripheral portions of the starting hexagonal colloid are milled in a second step.

**Non-linear photoluminescence microscopy.** A 180-fs pulsed Ti:Sapphire laser, with a repetition rate of 80 MHz, is used to generate the nonlinear photoluminescence of the metal. The laser beam is focused in a diffraction-limited spot by an oil-immersion aperture objective lens (N.A. 1.49). The focus diameter is estimated at 300 nm and the average power density at the sample is 20 mW. $\mu$ m<sup>-2</sup>. The polarization orientation of the incident light is controlled by a half-wavelength achromatic retardation plate. Two different nonlinear optical imaging modalities are implemented to obtain the modal landscape and the transmittance of the device as detailed in Supplementary Information.

**Simulations.** Numerical simulations of the local electromagnetic field, SP-LDOS and nPL signal were performed using home-made codes based on the 3D Green Dyadic Method as described in earlier reports.<sup>33</sup> The generalized propagator  $\mathbf{K}(\mathbf{r}, \mathbf{r}', \omega)$  is computed first that gives the total electromagnetic response of the complex metallic nanostructure under any arbitrary illumination field  $\mathbf{E}_0(\mathbf{R}_0, \mathbf{r}, \omega)$ . The double hexagon structure is discretized into hexagonal lattice of cells. The near-field transmittance calculations are performed with an excitation located at a fixed input co-ordinate (position vector  $\mathbf{r}_1$ ). The transmitted near-field intensity generated by the excited plasmonic field at a distal output co-ordinate (position vector  $\mathbf{r}_2$ ) is calculated. The energy transferred from input to output is obtained by solving the Dyson sequence equation which gives the Dyadic tensor  $\mathcal{S}(\mathbf{r}_2, \mathbf{r}_1, \omega)$ . Full details are given in Supplementary Information.

## ASSOCIATED CONTENT

### Supporting Information.

Supporting Information is available in the online version. The Supporting Information is available free of charge on the ACS Publications website at DOI:

Materials and Methods including details of confocal vs wide field microscopy (Fig. S1). SPLDOS and transmittance simulations and mapping (Fig. S2 and Supplementary Movie 1). Simulation of transmittance spectrum (Fig. S3). Digital and experimental nPL response images from the asynchronous double excitation of the double hexagon device (Fig. S4). Complete set of reconfigurable gates with  $110^\circ$  and  $150^\circ$  inputs (Fig. S5). nPL maps and intensity profiles used for Figure 3. (Fig. S6). Generalization to interconnect-free 3-bit reconfigurable logic units (Fig. S7). Calculation of near-field transmittance maps and spectra with two synchronous incident Gaussian beams. (Figs. S8, S9 and Supplementary Movie 2).

## AUTHOR INFORMATION

### Corresponding Author

\* Erik Dujardin. erik.dujardin@cemes.fr.

### ORCID

Upkar Kumar: 0000-0001-7645-6440

Aurélien Cuche: 0000-0002-1851-9578

Sviatlana Viarbitskaya: 0000-0002-4981-3251

Gérard Colas des Francs: 0000-0002-5097-7317

Sreenath Bolisetty: 0000-0002-1040-8945

Raffaele Mezzenga: 0000-0002-5739-2610

Alexandre Bouhelier: 0000-0002-0391-2836

Erik Dujardin: 0000-0001-7242-9250

## **Author Contributions**

ED, AB designed the experiments. RM, SB synthesized the Au microplatelets. UK, ED conducted the sample preparation and nanofabrication steps. AB, SV, RAR implemented the experimental optical set-ups. UK, SV, FDO performed the optical experiments. ED, UK processed the data. CG, AC, UK, GCdF developed the simulations tools and performed all GDM calculations. ED developed the gate mapping and drafted the manuscript, which was amended by all co-authors. All co-authors have given approval to the final version of the manuscript.

## **Notes**

The authors declare no competing financial interest.

## **ACKNOWLEDGEMENTS**

This work has been funded by the French Agence Nationale de la Recherche (ANR-13-BS10-0007-PLACORE), the European Research Council (ERC-2007-StG-203872-COMOSYEL), the Region of Burgundy (PARI II Photcom), the EIPHI graduate school (ANR-17-EUR-0002), the Conseil Régional de Bourgogne-Franche-Comté (APEX) and the European Regional Development Fund (Project Optiflex). The authors acknowledge the support of the massively parallel computing center CALMIP (Toulouse, Fr) through the project No P1107.

## REFERENCES

1. Salahuddin, S.; Ni, K.; Datta, S., The Era of Hyper-Scaling in Electronics. *Nat. Electron.* **2018**, *1* (8), 442-450.
2. Waldrop, M. M., The Semiconductor Industry Will Soon Abandon Its Pursuit of Moore's Law. Now Things Could Get a Lot More Interesting. *Nature* **2016**, *530* (7589), 144-147.
3. Kouzes, R. T.; Anderson, G. A.; Elbert, S. T.; Gorton, I.; Gracio, D. K., The Changing Paradigm of Data-Intensive Computing. *Computer* **2009**, *42* (1), 26-34.
4. Caulfield, H. J.; Dolev, S., Why Future Supercomputing Requires Optics. *Nat. Photonics* **2010**, *4* (5), 261-263.
5. Miller, D. A. B., Are Optical Transistors the Logical Next Step? *Nat. Photonics* **2010**, *4* (1), 3-5.
6. Veldhorst, M.; Yang, C. H.; Hwang, J. C. C.; Huang, W.; Dehollain, J. P.; Muhonen, J. T.; Simmons, S.; Laucht, A.; Hudson, F. E.; Itoh, K. M.; Morello, A.; Dzurak, A. S., A Two-Qubit Logic Gate in Silicon. *Nature* **2015**, *526* (7573), 410-414.
7. Kjaergaard, M.; Schwartz, M. E.; Braumuller, J.; Krantz, P.; Wang, J. I. J.; Gustavsson, S.; Oliver, W. D., Superconducting Qubits: Current State of Play. In *Annual Review of Condensed Matter Physics, Vol 11, 2020*, Marchetti, M. C.; Mackenzie, A. P., Eds. Annual Reviews: Palo Alto, 2020; Vol. 11, pp 369-395.
8. Fu, Y. L.; Hu, X. Y.; Lu, C. C.; Yue, S.; Yang, H.; Gong, Q. H., All-Optical Logic Gates Based on Nanoscale Plasmonic Slot Waveguides. *Nano Lett.* **2012**, *12* (11), 5784-5790.
9. Singh, P.; Tripathi, D. K.; Jaiswal, S.; Dixit, H. K., All-Optical Logic Gates: Designs, Classification, and Comparison. *Adv. Opt. Tech.* **2014**, 275083.
10. Zhang, M.; Wang, C.; Hu, Y. W.; Shams-Ansari, A.; Ren, T. H.; Fan, S. H.; Loncar, M., Electronically Programmable Photonic Molecule. *Nat. Photonics* **2019**, *13* (1), 36-40.
11. Han, B. C.; Liu, Y., All-Optical Reconfigurable Non-Inverted Logic Gates with a Single Semiconductor Optical Amplifier. *AIP Adv.* **2019**, *9* (1), 015007.
12. Wei, H.; Wang, Z. X.; Tian, X. R.; Kall, M.; Xu, H. X., Cascaded Logic Gates in Nanophotonic Plasmon Networks. *Nat. Commun.* **2011**, *2*, 387.
13. Borders, W. A.; Pervaiz, A. Z.; Fukami, S.; Camsari, K. Y.; Ohno, H.; Datta, S., Integer Factorization Using Stochastic Magnetic Tunnel Junctions. *Nature* **2019**, *573* (7774), 390-393.
14. Feldmann, J.; Youngblood, N.; Wright, C. D.; Bhaskaran, H.; Pernice, W. H. P., All-Optical Spiking Neurosynaptic Networks with Self-Learning Capabilities. *Nature* **2019**, *569* (7755), 208-214.
15. Landman, B. S.; Russo, R. L., Pin versus Block Relationship for Partitions of Logic Graphs. *IEEE Trans. Comput.* **1971**, *C 20* (12), 1469-1479.
16. Stroobandt, D., Recent Advances in System-Level Interconnect Prediction. *IEEE Circuits and Systems Society Newsletter* **2000**, *11* (4), 4-20.
17. Christie, P.; Stroobandt, D., The Interpretation and Application of Rent's Rule. *IEEE Trans. Very Large Scale Integr. (VLSI) Syst.* **2000**, *8* (6), 639-648.
18. Salem, R.; Foster, M. A.; Turner, A. C.; Geraghty, D. F.; Lipson, M.; Gaeta, A. L., Signal Regeneration Using Low-Power Four-Wave Mixing on Silicon Chip. *Nat. Photonics* **2008**, *2* (1), 35-38.
19. Nielsen, M. P.; Shi, X. Y.; Dichtl, P.; Maier, S. A.; Oulton, R. F., Giant Nonlinear Response at a Plasmonic Nanofocus Drives Efficient Four-Wave Mixing. *Science* **2017**, *358* (6367), 1179-1181.

20. Skidin, D.; Faizy, O.; Kruger, J.; Eisenhut, F.; Jancarik, A.; Nguyen, K. H.; Cuniberti, G.; Gourdon, A.; Moresco, F.; Joachim, C., Unimolecular Logic Gate with Classical Input by Single Gold Atoms. *ACS Nano* **2018**, *12* (2), 1139-1145.
21. Namarvar, O. F.; Giraud, O.; Georgeot, B.; Joachim, C., Quantum Hamiltonian Computing Protocols for Molecular Electronics Boolean Logic Gates. *Quantum Sci. Technol.* **2019**, *4* (3), 035009.
22. Dridi, G.; Namarvar, O. F.; Joachim, C., Qubits and Quantum Hamiltonian Computing Performances for Operating a Digital Boolean 1/2-Adder. *Quantum Sci. Technol.* **2018**, *3* (2), 025005.
23. Mahboob, I.; Flurin, E.; Nishiguchi, K.; Fujiwara, A.; Yamaguchi, H., Interconnect-Free Parallel Logic Circuits in a Single Mechanical Resonator. *Nat. Commun.* **2011**, *2*, 198.
24. Csaba, G.; Porod, W., Coupled Oscillators for Computing: A Review and Perspective. *Appl. Phys. Rev.* **2020**, *7* (1), 011302.
25. Silva, A.; Monticone, F.; Castaldi, G.; Galdi, V.; Alu, A.; Engheta, N., Performing Mathematical Operations with Metamaterials. *Science* **2014**, *343* (6167), 160-163.
26. Solli, D. R.; Jalali, B., Analog Optical Computing. *Nat. Photonics* **2015**, *9* (11), 704-706.
27. Molesky, S.; Lin, Z.; Piggott, A. Y.; Jin, W. L.; Vuckovic, J.; Rodriguez, A. W., Inverse Design in Nanophotonics. *Nat. Photonics* **2018**, *12* (11), 659-670.
28. Estakhri, N. M.; Edwards, B.; Engheta, N., Inverse-Designed Metastructures That Solve Equations. *Science* **2019**, *363* (6433), 1333-1338.
29. Koenderink, A. F.; Alu, A.; Polman, A., Nanophotonics: Shrinking Light-Based Technology. *Science* **2015**, *348* (6234), 516-521.
30. Ginis, V.; Piccardo, M.; Tamagnone, M.; Lu, J. S.; Qiu, M.; Kheifets, S.; Capasso, F., Remote Structuring of Near-Field Landscapes. *Science* **2020**, *369* (6502), 436-440.
31. Viarbitskaya, S.; Teulle, A.; Marty, R.; Sharma, J.; Girard, C.; Arbouet, A.; Dujardin, E., Tailoring and Imaging the Plasmonic Local Density of States in Crystalline Nanoprisms. *Nat. Mater.* **2013**, *12* (5), 426-432.
32. Teulle, A.; Bosman, M.; Girard, C.; Gurunatha, K. L.; Li, M.; Mann, S.; Dujardin, E., Multimodal Plasmonics in Fused Colloidal Networks. *Nat. Mater.* **2015**, *14* (1), 87-94.
33. Kumar, U.; Viarbitskaya, S.; Cuche, A.; Girard, C.; Bolisetty, S.; Mezzenga, R.; des Francs, G. C.; Bouhelier, A.; Dujardin, E., Designing Plasmonic Eigenstates for Optical Signal Transmission in Planar Channel Devices. *ACS Photonics* **2018**, *5* (6), 2328-2335.
34. Huang, J. S.; Callegari, V.; Geisler, P.; Bruning, C.; Kern, J.; Prangma, J. C.; Wu, X. F.; Feichtner, T.; Ziegler, J.; Weinmann, P.; Kamp, M.; Forchel, A.; Biagioni, P.; Sennhauser, U.; Hecht, B., Atomically Flat Single-Crystalline Gold Nanostructures for Plasmonic Nanocircuitry. *Nat. Commun.* **2010**, *1*, 150.
35. Viarbitskaya, S.; Demichel, O.; Cluzel, B.; des Francs, G. C.; Bouhelier, A., Delocalization of Nonlinear Optical Responses in Plasmonic Nanoantennas. *Phys. Rev. Lett.* **2015**, *115* (19), 197401.
36. Agreda, A.; Sharma, D. K.; Viarbitskaya, S.; Hernandez, R.; Cluzel, B.; Demichel, O.; Weeber, J. C.; des Francs, G. C.; Kumar, G. V. P.; Bouhelier, A., Spatial Distribution of the Nonlinear Photoluminescence in Au Nanowires. *ACS Photonics* **2019**, *6* (5), 1240-1247.
37. Feichtner, T.; Selig, O.; Hecht, B., Plasmonic Nanoantenna Design and Fabrication Based on Evolutionary Optimization. *Opt. Express* **2017**, *25* (10), 10828-10842.
38. Girard, C.; Wiecha, P. R.; Cuche, A.; Dujardin, E., Designing Thermoplasmonic Properties of Metallic Metasurfaces. *J. Opt.* **2018**, *20* (7), 075004.
39. Rewitz, C.; Razinskas, G.; Geisler, P.; Krauss, E.; Goetz, S.; Pawlowska, M.; Hecht, B.; Brixner, T., Coherent Control of Plasmon Propagation in a Nanocircuit. *Phys. Rev. Appl.* **2014**, *1* (1), 014007.

40. Wiecha, P. R.; Arbouet, A.; Girard, C.; Muskens, O. L., Deep Learning in Nano-Photonics: Inverse Design and Beyond. *Photonics Res.* **2021**, *9* (5), B182-B200.
41. Liu, D. J.; Tan, Y. X.; Khoram, E.; Yu, Z. F., Training Deep Neural Networks for the Inverse Design of Nanophotonic Structures. *ACS Photonics* **2018**, *5* (4), 1365-1369.
42. Hegde, R. S., Deep Learning: A New Tool for Photonic Nanostructure Design. *Nanoscale Adv.* **2020**, *2* (3), 1007-1023.
43. Dinsdale, N. J.; Wiecha, P. R.; Delaney, M.; Reynolds, J.; Ebert, M.; Zeimpekis, I.; Thomson, D. J.; Reed, G. T.; Lalanne, P.; Vynck, K.; Muskens, O. L., Deep Learning Enabled Design of Complex Transmission Matrices for Universal Optical Components. *ACS Photonics* **2021**, *8* (1), 283-295.
44. Wiecha, P. R.; Muskens, O. L., Deep Learning Meets Nanophotonics: A Generalized Accurate Predictor for Near Fields and Far Fields of Arbitrary 3D Nanostructures. *Nano Lett.* **2020**, *20* (1), 329-338.
45. Siampour, H.; Kumar, S.; Davydov, V. A.; Kulikova, L. F.; Agafonov, V. N.; Bozhevolnyi, S. I., On-Chip Excitation of Single Germanium Vacancies in Nanodiamonds Embedded in Plasmonic Waveguides. *Light-Sci. Appl.* **2018**, *7*, 61.
46. Kumar, U.; Bolisetty, S.; Mezzenga, R.; Girard, C.; Dujardin, E.; Cuche, A., Single Plasmon Spatial and Spectral Sorting on a Crystalline Two-Dimensional Plasmonic Platform. *Nanoscale* **2020**, *12* (25), 13414-13420.
47. Weeber, J. C.; Hammani, K.; Colas-des-Francis, G.; Bouhelier, A.; Arocas, J.; Kumar, A.; Eloi, F.; Buil, S.; Quelin, X.; Hermier, J. P.; Nasilowski, M.; Dubertret, B., Colloidal Quantum Dot Integrated Light Sources for Plasmon Mediated Photonic Waveguide Excitation. *ACS Photonics* **2016**, *3* (5), 844-852.
48. Uppu, R.; Pedersen, F. T.; Wang, Y.; Olesen, C. T.; Papon, C.; Zhou, X. Y.; Midolo, L.; Scholz, S.; Wieck, A. D.; Ludwig, A.; Lodahl, P., Scalable Integrated Single-Photon Source. *Sci. Adv.* **2020**, *6* (50), 6.
49. Lombardi, P.; Ovvyan, A. P.; Pazzagli, S.; Mazzamuto, G.; Kewes, G.; Neitzke, O.; Gruhler, N.; Benson, O.; Pernice, W. H. P.; Cataliotti, F. S.; Toninelli, C., Photostable Molecules on Chip: Integrated Sources of Nonclassical Light. *ACS Photonics* **2018**, *5* (1), 126-132.
50. Toninelli, C.; Gerhardt, I.; Clark, A. S.; Reserbat-Plantey, A.; Gotzinger, S.; Ristanovic, Z.; Colautti, M.; Lombardi, P.; Major, K. D.; Deperasinska, I.; Pernice, W. H.; Koppens, F. H. L.; Kozankiewicz, B.; Gourdon, A.; Sandoghdar, V.; Orrit, M., Single Organic Molecules for Photonic Quantum Technologies. *Nat. Mater.*, **2021**, *14*, DOI 10.1038/s41563-021-00987-4.
51. Cazier, N.; Buret, M.; Uskov, A. V.; Markey, L.; Arocas, J.; Des Francis, G. C.; Bouhelier, A., Electrical Excitation of Waveguided Surface Plasmons by a Light-Emitting Tunneling Optical Gap Antenna. *Opt. Express* **2016**, *24* (4), 3873-3884.
52. Cui, L. J.; Zhu, Y. X.; Abbasi, M.; Ahmadvand, A.; Gerislioglu, B.; Nordlander, P.; Natelson, D., Electrically Driven Hot-Carrier Generation and Above-Threshold Light Emission in Plasmonic Tunnel Junctions. *Nano Lett.* **2020**, *20* (8), 6067-6075.
53. Kullock, R.; Ochs, M.; Grimm, P.; Emmerling, M.; Hecht, B., Electrically-Driven Yagi-Uda Antennas for Light. *Nat. Commun.* **2020**, *11* (1), 7.
54. Wang, K.; Titchener, J. G.; Kruk, S. S.; Xu, L.; Chung, H. P.; Parry, M.; Kravchenko, I.; Chen, Y. H.; Solntsev, A. S.; Kivshar, Y. S.; Neshev, D. N.; Sukhorukov, A. A., Quantum Metasurface for Multiphoton Interference and State Reconstruction. *Science* **2018**, *361* (6407), 1104-1107.



# Interconnect-Free Multi-Bit Arithmetic and Logic Unit in a Single Reconfigurable 3- $\mu\text{m}^2$ Plasmonic Cavity

*Upkar Kumar<sup>1</sup>, Aurélien Cuche<sup>1</sup>, Christian Girard<sup>1</sup>, Sviatlana Viarbitskaya<sup>2</sup>, Florian Dell'Ova<sup>1,2</sup>, Raminfar Al Rafrain<sup>2</sup>, Gérard Colas des Francs<sup>2</sup>, Sreenath Bolisetty<sup>3</sup>, Raffaele Mezzenga<sup>3</sup>, Alexandre Bouhelier<sup>2</sup>, and Erik Dujardin<sup>1\*</sup>.*

<sup>1</sup> CEMES CNRS UPR 8011 and University of Toulouse, 29 rue J. Marvig, 31055 Toulouse, France.

<sup>2</sup> Laboratoire Interdisciplinaire Carnot de Bourgogne, CNRS UMR 6303, Université de Bourgogne Franche-Comté, 9 Av. A. Savary, 21000 Dijon, France.

<sup>3</sup> ETH Zurich, Department of Health Sciences and Technology, Schmelzberg-strasse 9, CH-8092 Zurich, Switzerland.

## SUPPORTING INFORMATION

- Materials and Methods (Fig. S1).	.....	<b>p. 2</b>
- SPLDOS and transmittance simulations and mapping and Supplementary Movie 1)	(Fig. S2 .....	<b>p. 5</b>
- Simulation of transmittance spectrum (Fig. S3)	.....	<b>p. 7</b>
- Digital and experimental nPL response maps from the asynchronous double excitation of the double hexagon device (Fig. S4)	.....	<b>p. 9</b>
- Complete set of reconfigurable gates with 110° and 150° inputs (Fig. S5)	.....	<b>p. 11</b>
- nPL maps and intensity profiles used for Figure 3. (Fig. S6)	.....	<b>p. 13</b>
- Generalization to interconnect-free 3-bit reconfigurable logic units. (Fig. S7)	.....	<b>p. 15</b>
- Calculation of near-field transmittance maps and spectra with two synchronous incident Gaussian beams. (Figs. S8, S9 and Supplementary Movie 2)	.....	<b>p. 17</b>

## Materials and Methods

The crystalline gold microplatelets studied here are synthesized using  $\beta$ -lactoglobulin protein fibrils according to the method reported in reference 1. Purified Beta-lactoglobulin protein monomer of 2 wt% is initially heat treated at 90°C and pH 2 condition for 5 hours resulting the formation of the multi-stranded amyloid fibrils. The microplatelets are prepared by mixing a 0.01M aqueous solution of  $\text{HAuCl}_4$  with 0.6 wt% solution of  $\beta$ -lactoglobulin fibrils. The solution is then heated at 55° C for 24 hours. The microplatelets are 20-40 nm in thickness and the typical in-plane dimensions are in the range of 1-15  $\mu\text{m}$ .

The colloidal suspension is drop-casted onto glass coverslips ( $22 \times 22 \times 0.15$  mm) coated with a nominal 10-nm indium-tin oxide (ITO) layer in order to evacuate charges during SEM imaging and FIB milling (*vide infra*). Cross-mark arrays are designed by photolithography and Au metallization. Organic residues are thoroughly washed with 10% aqueous ethanol solution and deionized water and the gold surface is decontaminated by three successive 5-min  $\text{O}_2$  plasma treatments.

The double hexagon structures are fabricated by focused ion milling of hexagonal microplatelets with diameter of 3-5  $\mu\text{m}$  using a gallium ion beam on a Zeiss 1540 XB dual beam microscope interfaced with a Raith Elphy Multibeam pattern generator. To ensure minimal substrate milling while thoroughly etching the gold, typical ion current of 1.0 pA and dose of 8000  $\mu\text{C}\cdot\text{cm}^{-2}$  are used. The milling protocol consists in etching out the double hexagon pattern first with minimal beam rastering along the double hexagon edges. The peripheral portions of the starting hexagonal colloid are milled in a second step.

The nonlinear photoluminescence of the metal is generated upon a pulsed laser excitation. We use a 180-fs pulsed Ti:Sapphire laser with a repetition rate of 80 MHz. The laser beam is focused in a diffraction-limited spot by an oil-immersion aperture objective lens (N.A. 1.49). The focus diameter is estimated at 300 nm and the average power density at the sample is 20  $\text{mW}\cdot\mu\text{m}^{-2}$ . The polarization orientation of the incident light is controlled by a half-wavelength achromatic retardation plate. In our measurement the nonlinearity exponent of the nonlinear photoluminescence integrated over the entire spectral detection window shows a near quadratic dependence and is assimilated as such in corresponding simulations.

Two different nonlinear optical imaging modalities are implemented to obtain the modal landscape and the transmittance of the device (Figure S1).

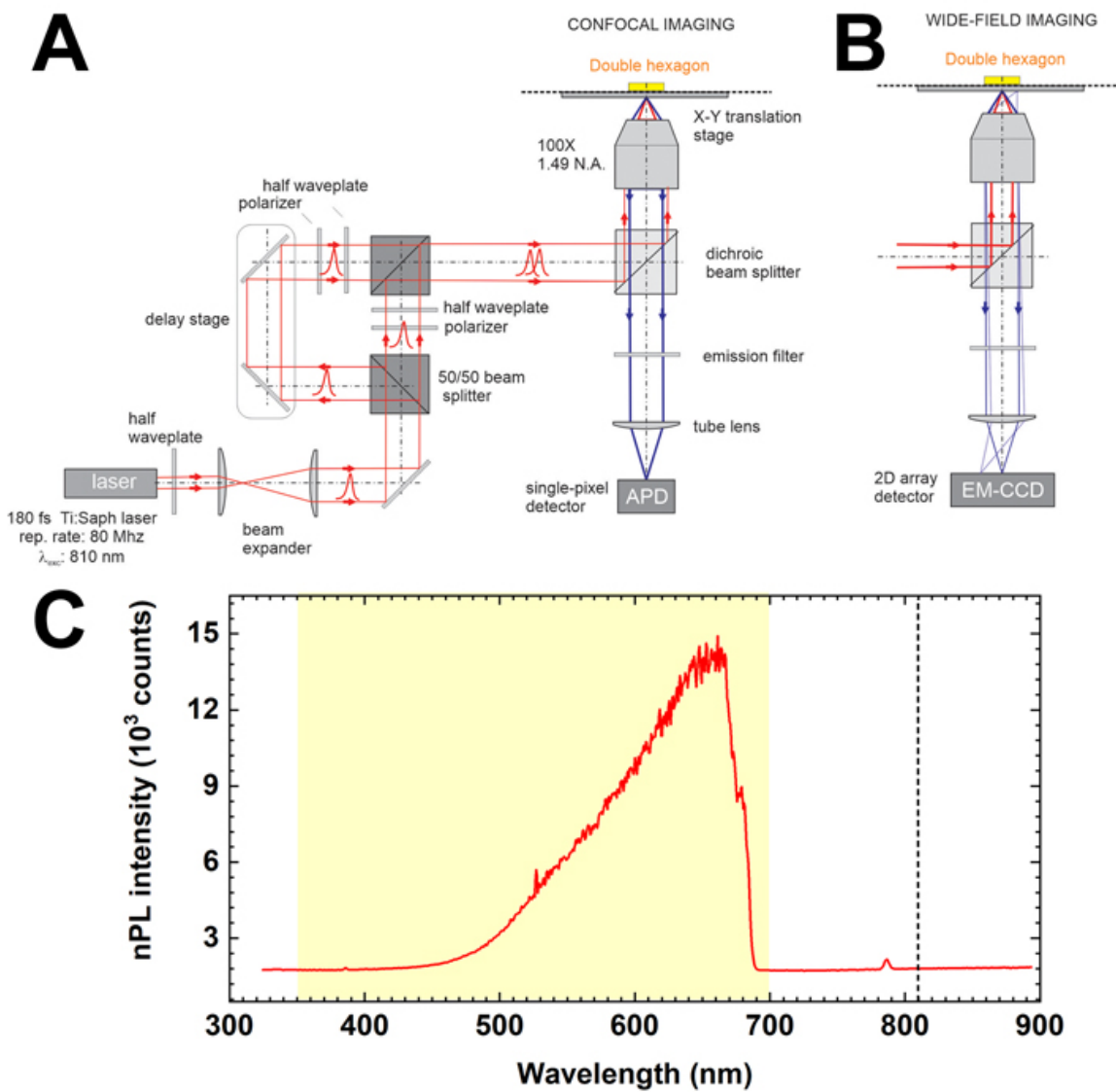


**Figure S1.** (A) Confocal nPL mapping set up. (B) Wide-field nPL imaging set-up. (C) Typical spectrum of the nPL signal as recorded in either confocal or wide-field configuration. The dotted line indicates the most commonly used excitation wavelength ( $\lambda = 810$  nm). The yellow area delineates the spectral range transmitted by the emission filter and over which the intensity is integrated.

The first implementation provides confocal maps reconstructed pixel-by-pixel by raster scanning the device through the focal spot with a two-dimensional piezoelectric stage. The nonlinear response is collected by the same objective and filtered in the 375–700 nm spectral range from the

backscattered fundamental beam by a dichroic beam splitter and a collection filter (Fig. S1A) and is detected by a single-photon avalanche photodiode counting module. The confocal nPL gives the strength of the response at particular excitation position, and to a reasonable approximation, is proportional to the squared in-plane surface plasmon local density of states (SP-LDOS).<sup>2</sup> The maps reveal the spatial distribution of the eigenmodes of the 2D confined plasmons (Figs. S3 and S4). In the second imaging modality (Fig. S1B), the nPL response of the entire device is recorded in a wide-field macroscopic image for a fixed excitation position to visualize the plasmon-mediated signal transfer and distant nPL generation within the device.<sup>3</sup>

In all the experimental work described here, the laser pulses emitted by the laser are split to form two arms where intensity and polarization of each can be independently adjusted. The pulses propagating in the two arms are then recombined before entering the optical microscope to form two focal spots, the position of which can be laterally controlled to overlap defined inputs of the double hexagon. A delay stage introduced in one arm allows us to control the temporal overlap between the two pulses. In the present report, the pulses are always arriving separately at their respective inputs.

## SPLDOS and transmittance simulations and mapping.

The double hexagon structure used to implement reconfigurable logic gates is obtained by Focused Ion Beam milling micrometer-wide and 40 nm thick single crystalline platelets. The final dimensions and morphology of the nanofabricated structure is characterized by scanning electron microscopy to create a mesh model that matches precisely the actual structure (Fig. S2A). The hexagonal compact mesh is composed of three layers of cells with lattice parameter of 10 nm. Our Green Dyadic Method (GDM) code is used to compute full or projected SPLDOS maps as illustrated in Fig. S2B where the SPLDOS enhancement along the peripheral edges is observed as well as the clear higher order mode modulation indicating that the structure is large enough to accommodate localized and delocalized modes.

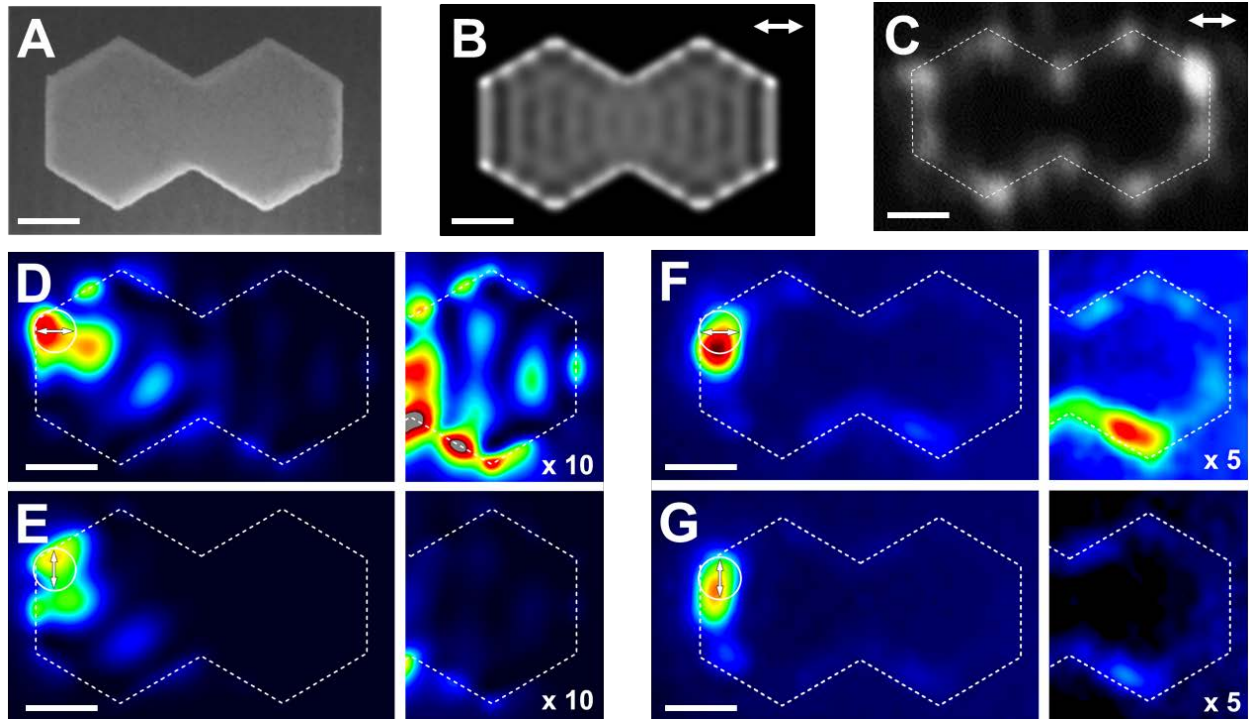


**Figure S2.** (A) SEM image of the FIB-milled double hexagon structure. (B) In-plane SPLDOS map for a horizontally polarized excitation at 810 nm. (C) Experimental confocal nPL map for a horizontally polarized excitation (beam waist 300 nm,  $\lambda = 810$  nm). (D, E) Simulated near-field transmittance map for a fixed horizontally (D) or vertically (E) polarized excitation in  $I_2$  (white circle). Beam waist 300 nm,  $\lambda = 810$  nm. The intensity in the right hexagon region is magnified ten times. (F, G) Experimental wide-field nPL maps for a fixed horizontally (F) or vertically (G) polarized excitation in  $I_2$  (white circle). Beam waist 300 nm,  $\lambda = 810$  nm. The intensity in the right hexagon region is magnified five times. Scale bars are 500 nm.

As shown in previous works, (31, 33) confocal nPL microscopy maps the squared in-plane SPLDOS convoluted with the Gaussian excitation beam. Figure S2C is obtained for a horizontally linearly polarized excitation and show a series of bright spots along the perimeter of the structure with little signal coming from the core of the hexagons, in good agreement with the SPLDOS map calculated for the same excitation polarization in Fig. S2B. These SPLDOS and confocal nPL maps indicate that the apexes exhibit an enhanced SPLDOS that can be used as effective excitation inputs or emissive nPL output.

Using the modified numerical GDM tool developed in ref (33), we simulate near-field transmission maps obtained for an excitation with a single Gaussian beam placed and fixed in the input location. Equivalently, one can consider the model described in page 17 with  $E_2 = 0$ . In Figures S2D-G, the transmitted near-field is shown when the upper left apex of the left hexagon is excited with a 300 nm Gaussian beam (white circle). When the laser is linearly polarized along the horizontal direction(Fig. S2D), a significant field ( $\sim 5-10\%$ ) is obtained in the distal region of the right hexagon. When the polarization is rotated to  $90^\circ$ , as shown in Fig. S2E the transmittance in the right side region is significantly suppressed.

Experimentally, the transmitted signal is better detected in wide field nPL experiments where the excitation beam is parked in a fixed position and the response of the entire plasmonic structure is recorded in wide-field microscopy (See page 2 and Fig. S1). This is clearly shown in Figs. S2F and S2G which exhibit essentially the same features as the simulated near-field transmittance maps, including the  $0^\circ / 90^\circ$  polarization dependency (see also Figs. 2D and 2E or Fig. S3B and S3C for other polarization configurations); The very good agreement between simulated transmittance and wide field mapping confirms the relevance of our theoretical approach.(33)

Additionally, Supplementary Movie 1 shows the evolution of the wide field nPL maps when the incident polarization of the excitation beam parked in  $I_3$  is rotated for excitation wavelength at 810 and 750 nm successively.

### Simulation of transmittance spectrum.

The near-field transmittance GDM tool used for the map in FigS1D can also be used to calculate transmittance spectra. In Figure S3, we consider an excitation by a single Gaussian beam in input  $I_3$  with a linear polarization at  $70^\circ$ . The experimental wide field nPL image (Fig. S3B) obtained for an excitation wavelength of 810 nm shows that a significant signal is produced at the apex  $O_1$ . This remote nPL emission in  $O_1$  is suppressed in the experimental map obtained when the excitation polarization is rotated to  $130^\circ$  (Fig. S3C). We calculate the near-field transmittance spectrum between  $I_3$  (excitation input) and  $O_1$  (readout output), i. e. the near-field intensity recorded in  $O_1$  for a single fixed Gaussian excitation in  $I_3$  as the excitation wavelength is scanned between 600 and 900nm (Fig. S3D). When the excitation is linearly polarized at  $70^\circ$ , the transmittance presents two clear resonance peaks centered at 710 and 810 nm. The transmittance is strongly suppressed over the entire spectral window, when the polarization is rotated at  $130^\circ$  in agreement with the low intensity observe in  $O_1$  in Fig. S3C. The calculated transmittance spectrum suggests that the excitation wavelength of 810 nm used in Figs. 1 and 2 is close to optimal for Boolean inputs encoded with  $70^\circ$  and  $130^\circ$  polarizations.

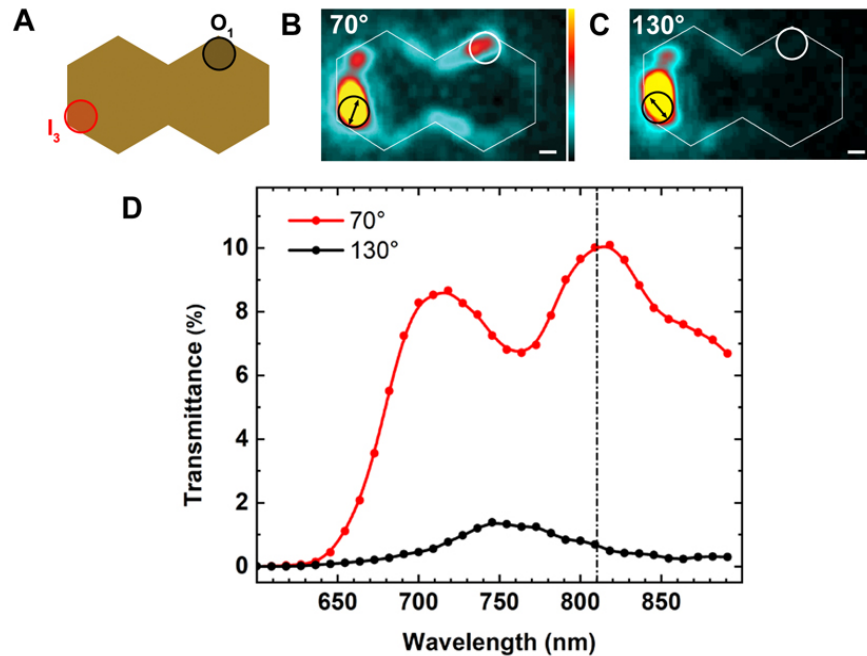


**Figure S3.** (A) Sketch of the double hexagon structure with fixed excitation at apex  $I_3$  with a 300-nm diameter Gaussian beam and location of the output area  $O_1$ . (B, C) Experimental wide-field nPL maps of the double hexagon excited in  $I_3$  ( $\lambda = 810$  nm) with a tightly focused laser beam linearly polarized at (B)  $70^\circ$  and (C)  $130^\circ$ . The white circle indicates the area of output  $O_1$ . (D) Simulated near-field transmittance spectrum recorded in  $O_1$  for an excitation in  $I_3$  polarized at  $70^\circ$  (red) and  $130^\circ$  (black).

**Digital and experimental nPL response maps from the asynchronous double excitation of the double hexagon device.**

In order to validate the construction of the 2-input logic gate response map from single excitation nPL wide-field maps, as used throughout this work, we have considered exciting the double hexagon structure, shown in Figure S4A, in inputs  $I_0$  and  $I_5$  with  $0^\circ$  polarization. The nPL response of the device to a single beam excitation in either  $I_0$  or  $I_5$  is shown in Fig. S4B and Fig. S4C respectively. The numerical sum of these two maps is displayed in Figure S4D.

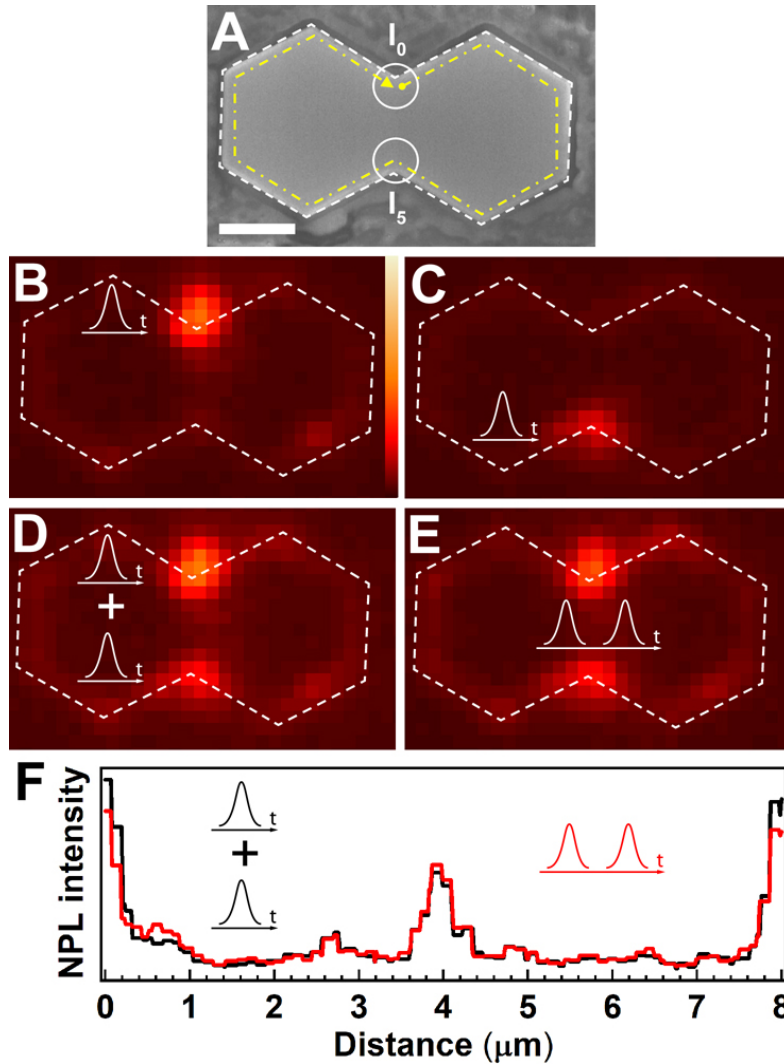


**Figure S4.** (A) SEM and (B,C) wide-field nPL maps of the double hexagon excited in  $I_0$  (top) or  $I_5$  (bottom) input respectively. (D) Numerical sum of maps (B) and (C). (E) Wide-field nPL maps recorded by cumulatively the response obtained by the asynchronous excitation of both  $I_0$  and  $I_5$ . (F) nPL intensity profiles of (D), in black, and (E), in red, along the path shown by the dash-dotted yellow line in (A) from dot to arrowhead.

A modification of the experimental excitation scheme allowed us to split the pulsed excitation in two beams that were focused in  $I_0$  and  $I_5$  so that individual pulses arrived at one input when the other was not excited (See page 2, Figure S1). The nPL map recorded during such an asynchronous double excitation is shown in Figure S4E. The exact similarity of both numerical summation and asynchronous double excitation is clearly visible and further evidenced by plotting the nPL intensity profiles from Figures S4D and S4E along the entire perimeter of the double hexagon as shown in Figure S4F. The perfect overlap of both profiles confirms that the incoherent logic gate response to a 2-input excitation can be constructed from the numerical summation of two single input excitation maps.

Complete set of reconfigurable gates with 110° and 150° input Boolean encoding.

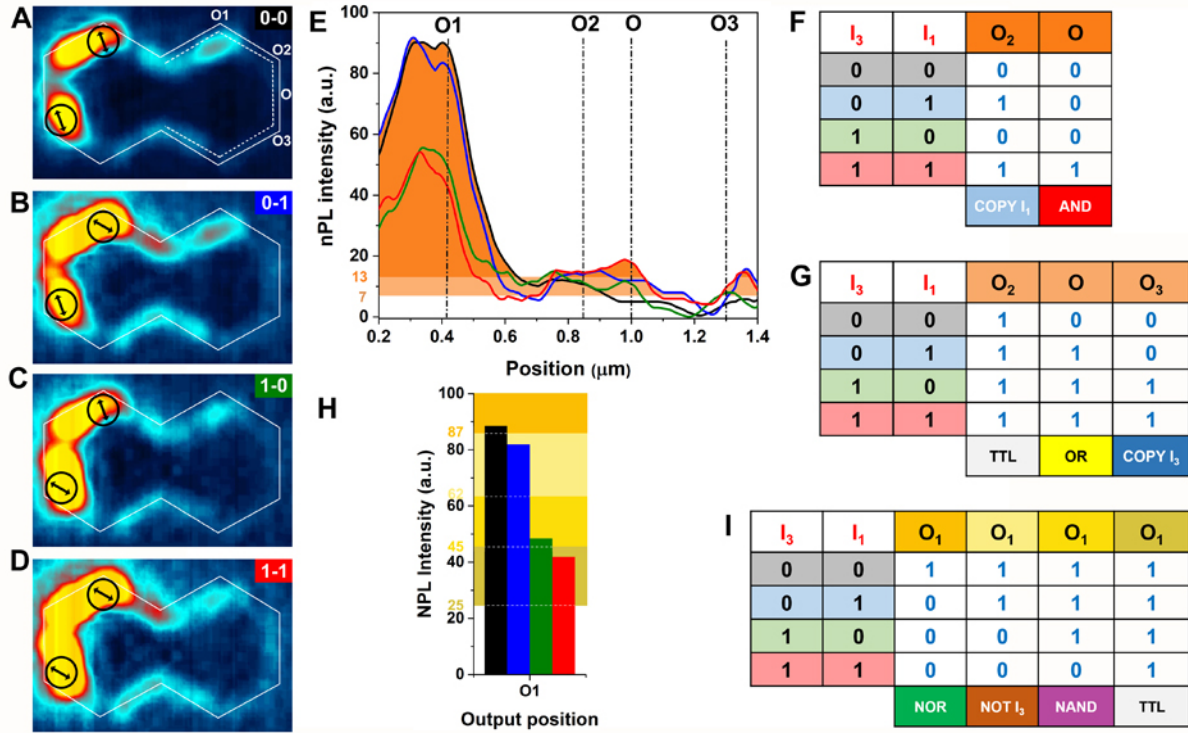


**Figure S5.** (A-D) Experimental non-coherent response of the double hexagon structure constructed from the wide-field nPL maps obtained for fixed excitation in  $I_3$  and  $I_1$  with a focused beam polarized at 110° ("0") or 150° ("1"). (A) ( $I_3; I_1$ ) = ("0";"0"). (B) ( $I_3; I_1$ ) = ("0";"1"). (C) ( $I_3; I_1$ ) = ("1";"0"). (D) ( $I_3; I_1$ ) = ("1";"1"). (E) Intensity profiles extracted along the dashed line on the perimeter of the right hexagon from (A-D) in black, blue, green and red respectively. Signal exceeding thresholds of 9 and 17 are indicated in light and dark orange. (F, G) Boolean output in  $O$ ,  $O_2$  and  $O_3$  for (F) threshold 13 and (G) threshold 7. (H) Histogram representation of the intensity values in  $O_1$  (See panel (E) at position 0.41  $\mu\text{m}$ ) compared to threshold levels 87, 62, 45 and 25. (I) Boolean output in  $O_1$  for the four thresholds NOR at 87, NOT  $I_3$  for 62, NAND for 45 and TTL for 25.

Figure S5 collects an entirely independent set of reconfigurable gates similar to the one shown and detailed in Figure 2 but obtained, on the same double hexagon structure, using 110° and 150° to encode the Boolean "0" and "1" inputs and  $I_1$  and  $I_3$  as input ports. The asynchronous response of the device to the four excitation configurations (0-0, 0-1, 1-0, 1-1) is shown in panels (A)-(D) from which the intensity profiles along the perimeter of the right hexagon are extracted and plotted in panel (E). The output ports  $O$ ,  $O_2$  and  $O_3$  shown in Fig. S5A realize the gates AND, Copy  $I_1$  for threshold 13 (Fig. S5F) and can be reconfigured into OR, Tautology, Copy  $I_3$  for threshold 7 (Fig. S5G). The output  $O_1$  alone implements four different gates (NOR, NOT, NAND and TTL)

as the threshold is swept from 87 to 62 to 45 to 25 (Figs. S5H, S5I). Outputs  $O_2$  and  $O_3$  can be reconfigured to the Contradiction gate for any threshold exceeding 30. Note that the data of output  $O_1$  at threshold 45 is displayed in Figures 3A and 3B.

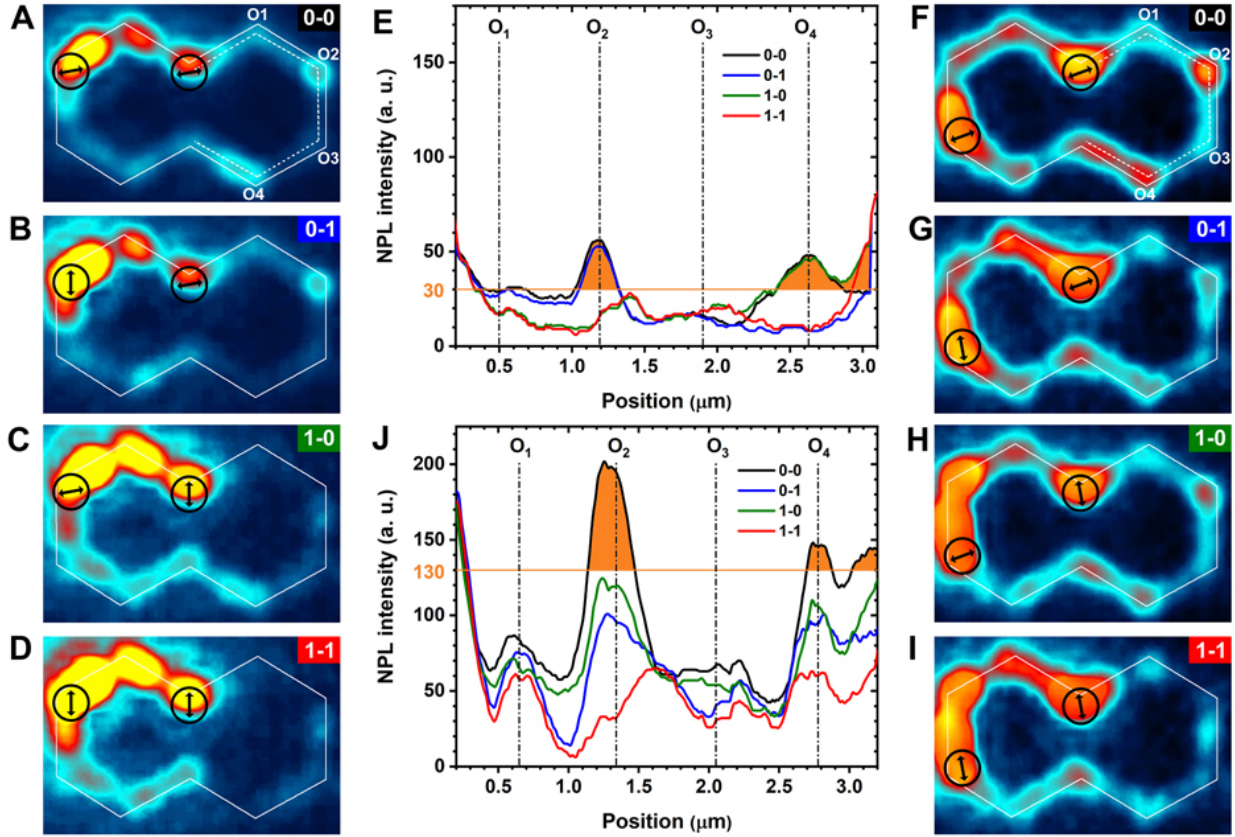
### **nPL maps and intensity profiles used for Figure 3.**

Figure 3 presents three reconfiguration modes to obtain new Boolean logic gates from the same double hexagon structure introduced in Figures 1 and 2. In particular, changing the set of polarization directions used to encode the Boolean inputs, while keeping the input locations and excitation wavelength is shown in Figures 3A and 3B. Changing the set of input locations is examined in Figures 3C and 3D. Finally, the excitation of the device at another energy ( $\lambda_{\text{exc}} = 750 \text{ nm}$ ) that mobilizes a new set of plasmon modes resulting in new transmittance patterns is illustrated in Figure 3E and 3F. The data shown in Figure 3 as nPL intensity histograms associated with the four Boolean input configurations (0-0, 0-1, 1-0, 1-1), for each considered output port (typically  $O_1$  through  $O_5$ ), are extracted from wide field nPL transmittance maps as explained for Figure 2, with the corresponding excitation/readout parameters.

The experimental wide field nPL transmittance maps and intensity profiles used in Figs. 3A,B are given in Figure S5A-D and S5E respectively.

Figures S6A to S6D present the wide field nPL transmittance maps when the double hexagon is excited in inputs  $I_0$  and  $I_2$  with a wavelength of 810 nm and polarization directions of  $10^\circ$  and  $90^\circ$  to encode the input "0" and "1". The nPL transmittance intensity along the dotted line linking the output ports  $O_1$  to  $O_5$  is shown in Figure S6E. The main text focuses on outputs  $O_2$  and  $O_4$ , which are reconfigured into NOT( $I_0$ ) and NOT( $I_2$ ) gate functions for a threshold of 30, from their initial COPY gate function in Figure 2.

Similarly, Figures S6F to S6I display the experimental wide field nPL transmittance maps for the four excitation configurations of the double hexagon in inputs  $I_0$  and  $I_3$  with a 750 nm laser polarized along the  $20^\circ$  or  $100^\circ$  directions to encode the input "0" and "1" respectively. The nPL transmittance intensity along the dotted line in Fig. S6F are gathered in Figure S6J. When one chooses a threshold of 130, output ports  $O_2$  and  $O_4$  are now reconfigured into a universal NOR gate. The exact same data for these two outputs are shown as histograms in Figure 3E.



**Figure S6.** Reconfiguration of the Boolean function of the double hexagon device. (A-E) Choosing the input locations. Data corresponding to Boolean operation shown in Figs. 3C-D where inputs  $I_0$  and  $I_2$  are excited at 810 nm with polarizations  $10^\circ$  and  $90^\circ$  encoding the "0" and "1" Boolean inputs. Response maps (A) to (D) are constructed from the four corresponding wide field nPL maps. The device readout is performed along the dotted line shown in (A) and displayed in panel (E). When a readout threshold of 30 is chosen, the device performs NOT( $I_0$ ) and NOT( $I_2$ ) in the output  $O_2$  and  $O_4$  respectively. (F-J) Choosing the excitation energy. Data shown in Figs. 3E-F are obtained by exciting the double hexagon in inputs  $I_0$  and  $I_3$  at 750 nm with polarizations  $20^\circ$  and  $100^\circ$  encoding the "0" and "1" Boolean inputs. Response maps (F) to (I) are constructed from the four corresponding nPL maps. (J) Response profiles along the dotted line in (F). When a readout threshold of 130 is chosen, outputs  $O_2$  and  $O_4$  are reconfigured to the universal NOR gate.

### Generalization to interconnect-free 3-bit reconfigurable logic units.

Mimicking interconnect-free Application-Specific Integrated Circuits (ASIC), DH plasmonic cavities can perform specific Boolean operations with  $N > 2$  inputs.

Figure S7 demonstrates this generalization to a higher level of complexity by directly extending, without any optimization or adjustment, the principles described in the main text to reach 3-input reconfigurable logic units. In this example, input  $I_4$  is considered alongside the two inputs  $I_1$  and  $I_3$  studied in Figure 2. The DH response maps corresponding to the  $2^3 = 8$  possible excitation configurations using the same  $70^\circ$  and  $130^\circ$  polarizations to encode "0" and "1" Boolean inputs are shown in Figures S7A to S7H.

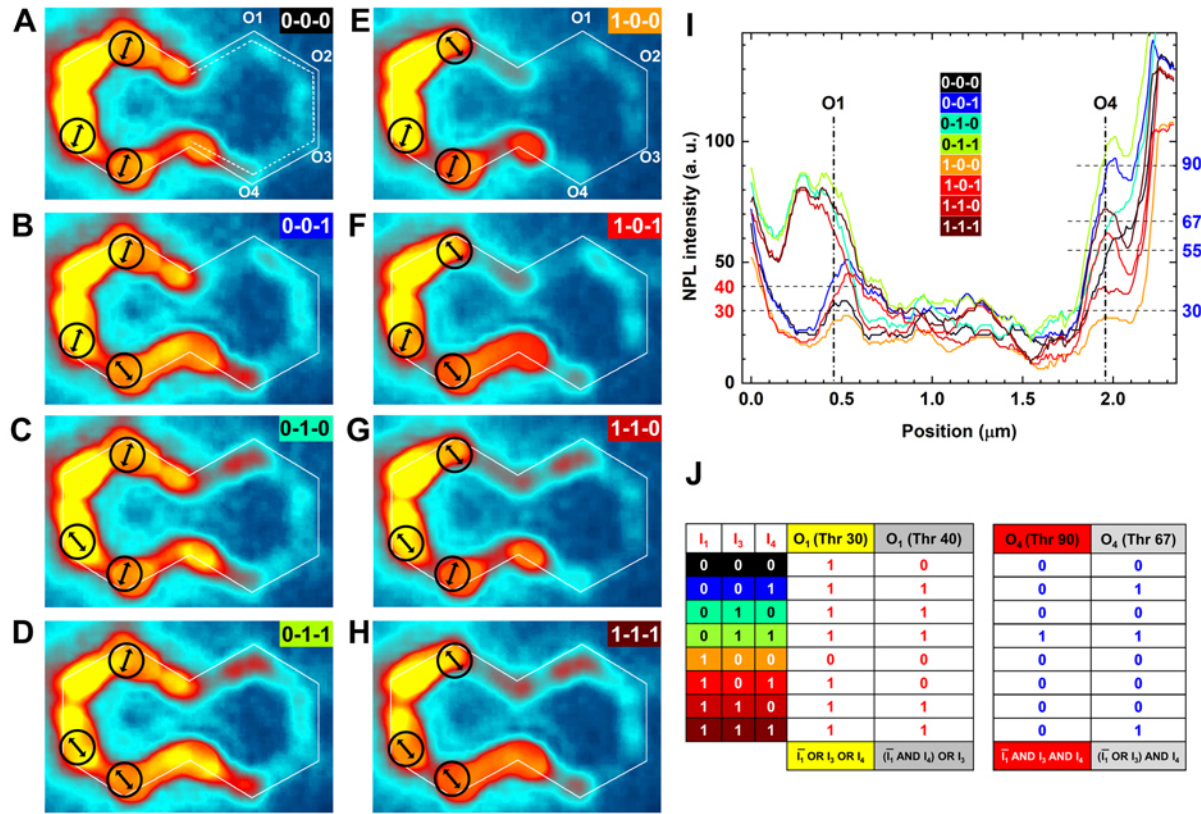


**Figure S7.** DH cavity operated as a 3-bit ASIC-like reconfigurable logic unit producing non trivial Boolean functions. (A-H) Experimental non-coherent responses of the double hexagon structure constructed from the wide-field nPL maps obtained for fixed excitation in  $I_1$ ,  $I_3$  and  $I_4$  with a focused beam polarized at  $70^\circ$  ("0") or  $130^\circ$  ("1"). (A) ( $I_1$ ;  $I_3$ ;  $I_4$ ) = ("0"; "0"; "0"). (B) ( $I_1$ ;  $I_3$ ;  $I_4$ ) = ("0"; "0"; "1"). (C) ( $I_1$ ;  $I_3$ ;  $I_4$ ) = ("0"; "1"; "0"). (D) ( $I_1$ ;  $I_3$ ;  $I_4$ ) = ("0"; "1"; "1"). (E) ( $I_1$ ;  $I_3$ ;  $I_4$ ) = ("1"; "0"; "0"). (F) ( $I_1$ ;  $I_3$ ;  $I_4$ ) = ("1"; "0"; "1"). (G) ( $I_1$ ;  $I_3$ ;  $I_4$ ) = ("1"; "1"; "0"). (H) ( $I_1$ ;  $I_3$ ;  $I_4$ ) = ("1"; "1"; "1"). (I) Intensity profiles extracted along the dashed line on the perimeter of the right hexagon from (A-H). (J) Complex Boolean outputs in  $O_1$  (resp.  $O_4$ ) for the thresholds 30 and 40 (resp. 90 and 67) that can be associated to the logic functions displayed in the last line. NOT( $I_1$ ) is noted as  $\bar{I}_1$ .

In Figure S7I, the DH response in the rightmost area is explored by plotting the eight NPL transmittance profiles along the dotted line in Fig. S7A. The tables of truth of four different 3-bit ASIC-like Boolean functions are displayed in Figure S7J. At readout threshold 30, the Boolean response at output  $O_1$  is  $\overline{I_1} OR I_3 OR I_4$ , which, except for the inversion of  $I_1$ , is equivalent to a 3-bit OR gate. Similarly, the output  $O_4$  read at threshold 90 yields a quasi 3-bit AND gate with the response  $\overline{I_1} AND I_3 AND I_4$ . But also the quasi 3-bit OR ( $\overline{I_1} OR I_3 OR I_4$ ) at threshold 30. Other 3-bit Boolean functions combining OR and AND gates are obtained without cascades nor redesigning the DH cavity but by the simple adjustment of the readout threshold. At threshold 40,  $O_1$  produces the Boolean function  $(\overline{I_1} AND I_4) OR I_3$ , when  $O_4$  implements a complementary Boolean operation,  $(\overline{I_1} OR I_3) AND I_4$  at threshold 67. Incidentally,  $O_4$  also implements  $(\overline{I_1} AND I_3) OR I_4$  at threshold 55.

These examples demonstrate that the adequate exploitation of the modal landscape inscribed in the DH cavity allows to realize not only simple 2-bit gates but also more complex multibit logic functions at fixed energy (here  $\lambda = 810$  nm), without necessitating to create a new plasmonic device or to concatenate it to another, which would raise issues of dissipation.

## Calculation of near-field transmittance maps and spectra with two synchronous incident Gaussian beams.

Here, we describe the numerical tool based on the Green dyadic formalism that provides the computation of the electric field transfer between two distinct input locations and a remote output location in an arbitrary shaped metallic nanostructure as illustrated in Figure S8.

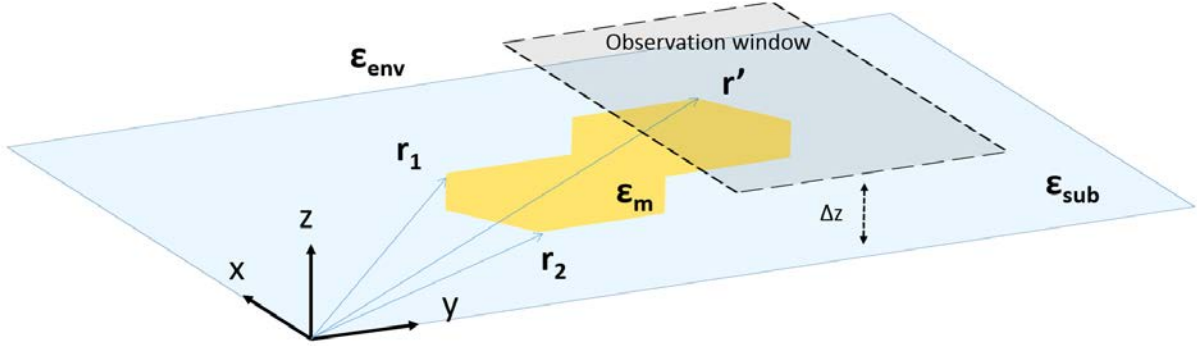


**Figure S8.** Schematic geometry of a plasmonic 2D double hexagon device supported by a transparent dielectric substrate, and the associated observation window used for simulations which is positioned above the structure. The size of this window can be adjusted.

In a metallic system where surface plasmons are excited by a bi-focused illumination  $\mathbf{E}_0 = \mathbf{E}_1 + \mathbf{E}_2$ , of angular frequency  $\omega$  and positioned at  $\mathbf{r}_1$  and  $\mathbf{r}_2$ , the expression of the electric field  $\mathbf{E}_{out}$  at a given output location  $\mathbf{r}'$  can be expressed as follows:<sup>4,5</sup>

$$\mathbf{E}_{out}(\mathbf{r}', \mathbf{r}_1, \mathbf{r}_2, \omega) = \int_V \mathbf{K}(\mathbf{r}', \mathbf{r}, \omega) \cdot \mathbf{E}_0(\mathbf{r}, \mathbf{r}_1, \mathbf{r}_2, \omega) d, \mathbf{r} \quad (1)$$

where  $V$  is the volume of the metallic object, and  $\mathbf{K}(\mathbf{r}', \mathbf{r}, \omega)$  is the generalized field propagator that contains the entire response of the sample under any incident illumination:<sup>4</sup>

$$\mathbf{K}(\mathbf{r}', \mathbf{r}, \omega) = \mathbf{I}\delta(\mathbf{r} - \mathbf{r}') + \chi(\mathbf{r}, \omega) \cdot \mathbf{S}(\mathbf{r}', \mathbf{r}, \omega) \quad (2)$$

$\mathbf{S}(\mathbf{r}', \mathbf{r}, \omega)$  is the Green Dyadic tensor describing the whole system that includes the plasmonic structure and the dielectric substrate, and  $\mathbf{I}$  is the identity matrix. In addition, the frequency-dependent optical response of the metallic structure is given by:

$$\chi(\mathbf{r}, \omega) = \frac{\varepsilon_m(\mathbf{r}, \omega) - \varepsilon_{env}}{4\pi} \quad \text{in the metal,} \quad (3)$$

and

$$\chi(\mathbf{r}, \omega) = 0 \quad \text{outside of the metallic object.}$$

In this work, we focus on the plasmon-mediated field transfer in the metallic structures. We therefore exclude the direct contribution of the bi-focused incident illumination at the output location.<sup>6</sup> This can be done by removing the delta Dirac distribution in equation (2):

$$\mathbf{K}(\mathbf{r}', \mathbf{r}, \omega) = \chi(\mathbf{r}, \omega) \cdot \mathbf{S}(\mathbf{r}', \mathbf{r}, \omega) \quad (4)$$

The whole set of experimental data presented in this study has been acquired using two asynchronous focused Gaussian illuminations. In Figure 4, we consider that the two beams coherently excite the structure in the final section. Consequently, each spots  $\mathbf{E}_1$  and  $\mathbf{E}_2$  has been modelled as a Gaussian spot through a plane waves expansion in the wave vector domain for each contribution:<sup>7-10</sup>

$$\mathbf{E}_j(\mathbf{r}, \mathbf{r}_j, \omega) = \int_{-\sqrt{\varepsilon_{sub}k_0}}^{\sqrt{\varepsilon_{sub}k_0}} d\alpha \int_{-\sqrt{\varepsilon_{sub}k_0^2 - \alpha^2}}^{\sqrt{\varepsilon_{sub}k_0^2 - \alpha^2}} d\beta \zeta \exp(i\Delta\Phi_j) \exp\left[-\frac{w_0^2(\alpha^2 + \beta^2)}{4}\right] \exp[i\alpha(x - x_j) + i\beta(y - y_j) + ik_z(z - z_j)], \quad (5)$$

$k_0$  is the vacuum wave vector of the incident light and  $\mathbf{r}_j = (x_j, y_j, z_j)$  defines the center of the  $j^{th}$  excitation Gaussian spot in the Cartesian system of coordinates shown in Fig. S8.  $\varepsilon_{sub}$  is the dielectric function of the substrate and the beam waist  $w_0$  describes the lateral extension of the two similar incident Gaussian beams.  $\Delta\Phi_j = \Phi_j - \Phi_1$  is the relative phase between the light beam  $\mathbf{E}_j$  and the light beam  $\mathbf{E}_1$ . So  $\Delta\Phi_1 = 0$  and  $\Delta\Phi_2 = \Phi_2 - \Phi_1$ .

The integration in equation (5) is performed in the 2D reciprocal space defined by the vector  $\mathbf{k}_{//} = (\alpha, \beta)$ . In order to take into account the realistic geometry of the system with a transparent substrate, for a given Gaussian spot, the tangential components of the total field vector  $\zeta$  are expressed as follows:

$$\begin{pmatrix} \zeta_x \\ \zeta_y \end{pmatrix} = \mathbf{T} \begin{pmatrix} E_x \\ E_y \end{pmatrix}, \quad (6)$$

The transmission matrix  $\mathbf{T}$  reads:

$$\mathbf{T} = \begin{pmatrix} (\tau_{//} - \tau_{\perp}) \cos^2 \delta + \tau_{\perp} & (\tau_{//} - \tau_{\perp}) \cos \delta \sin \delta \\ (\tau_{//} - \tau_{\perp}) \cos \delta \sin \delta & (\tau_{//} - \tau_{\perp}) \sin^2 \delta + \tau_{\perp} \end{pmatrix}, \quad (7)$$

$\tau_{\parallel}$  and  $\tau_{\perp}$  are the Fresnel coefficients for the interface. Here,  $\delta$  is an angle in the  $xy$  plane between the  $x$ -axis in Cartesian coordinates and the orientation of the planar component of the wave vector  $\mathbf{k}_{\parallel}$ .

In equation (5), the normal component  $\zeta_z$  of  $\zeta$  is obtained using the following expression:

$$\zeta_z = -(\alpha\zeta_{inc,x} + \beta\zeta_{inc,y}) / (\epsilon_{sub}k_0^2 - \alpha^2 - \beta^2)^{1/2} \quad (8)$$

Finally, the electric intensity distributions generated in the simulated maps of the main manuscript and in Figure S9 take the following form:

$$I_{out}(\mathbf{r}', \mathbf{r}_1, \mathbf{r}_2, \omega) = |\mathbf{E}_{out}(\mathbf{r}', \mathbf{r}_1, \mathbf{r}_2, \omega)|^2 \quad (9)$$

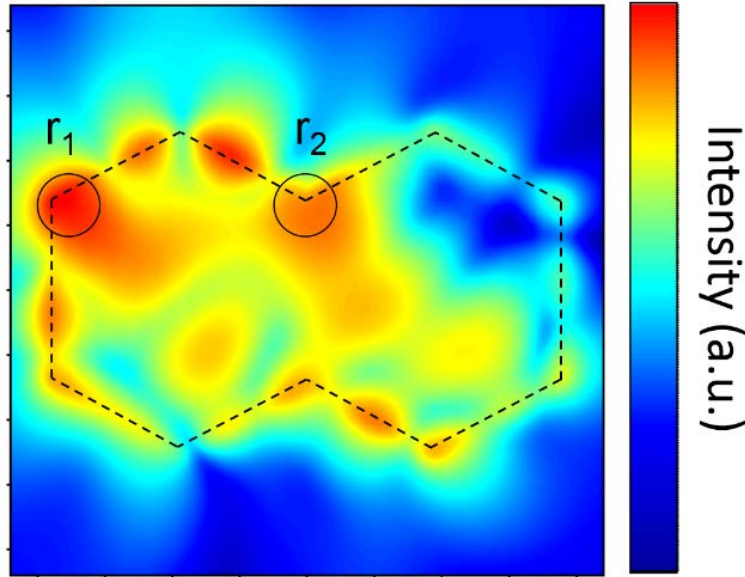


**Figure S9.**  $2 \times 2 \mu\text{m}^2$  simulated images showing the normalized intensity distribution ( $I_{out}$ ) above the double hexagon device under coherent excitation by two Gaussian beams in  $\mathbf{r}_1$  and  $\mathbf{r}_2$ . The positions of the two excitation spots are indicated by the black circles. The polarization is  $150^\circ$  for both spots, and the phase difference is  $\Delta\Phi = 60^\circ$ .

The effect of the phase difference  $0 \leq \Delta\Phi \leq 360^\circ$  is shown in Supplementary Movie 2 where each panel describes one polarization set -  $(110^\circ, 110^\circ)$ ,  $(110^\circ, 150^\circ)$ ,  $(150^\circ, 110^\circ)$  or  $(150^\circ, 150^\circ)$  - and is animated as the phase difference is scanned through. The clear sweep of intensity due to the destructive and constructive plasmon interferences leads to the production of the non-trivial XOR and NXOR transmittance relationships exploited in Figure 4 in the main text.

## References

1. Li, C. X.; Bolisetty, S.; Mezzenga, R., Hybrid Nanocomposites of Gold Single-Crystal Platelets and Amyloid Fibrils with Tunable Fluorescence, Conductivity, and Sensing Properties. *Adv. Mater.* **2013**, *25* (27), 3694-3700.
2. Viarbitskaya, S.; Teulle, A.; Marty, R.; Sharma, J.; Girard, C.; Arbouet, A.; Dujardin, E., Tailoring and Imaging the Plasmonic Local Density of States in Crystalline Nanoprisms. *Nat. Mater.* **2013**, *12* (5), 426-432.
3. Viarbitskaya, S.; Demichel, O.; Cluzel, B.; des Francs, G. C.; Bouhelier, A., Delocalization of Nonlinear Optical Responses in Plasmonic Nanoantennas. *Phys. Rev. Lett.* **2015**, *115* (19), 197401.
4. Martin, O. J. F.; Girard, C.; Dereux, A., Generalized Field Propagator for Electromagnetic Scattering and Light Confinement. *Phys. Rev. Lett.* **1995**, *74* (4), 526-529.
5. Barchiesi, D.; Girard, C.; Martin, O. J. F.; VanLabeke, D.; Courjon, D., Computing the Optical Near-Field Distributions around Complex Subwavelength Surface Structures: A Comparative Study of Different Methods. *Phys. Rev. E* **1996**, *54* (4), 4285-4292.
6. Arbouet, A.; Mlayah, A.; Girard, C.; des Francs, G. C., Electron Energy Losses and Cathodoluminescence from Complex Plasmonic Nanostructures: Spectra, Maps and Radiation Patterns from a Generalized Field Propagator. *New J. Phys.* **2014**, *16*, 14.
7. Torok, P.; Varga, P.; Booker, G. R., Electromagnetic Diffraction of Light Focused through a Planar Interface between Materials of Mismatched Refractive Indexes - Structure of The Electromagnetic Field .1. *J. Opt. Soc. Am. A-Opt. Image Sci. Vis.* **1995**, *12* (10), 2136-2144.
8. Torok, P.; Varga, P.; Konkol, A.; Booker, G. R., Electromagnetic Diffraction of Light Focused through a Planar Interface between Materials of Mismatched Refractive Indices: Structure of the Electromagnetic Field .2. *J. Opt. Soc. Am. A-Opt. Image Sci. Vis.* **1996**, *13* (11), 2232-2238.
9. Weeber, J. C.; Dereux, A.; Girard, C.; Krenn, J. R.; Goudonnet, J. P., Plasmon Polaritons of Metallic Nanowires for Controlling Submicron Propagation of Light. *Phys. Rev. B* **1999**, *60* (12), 9061-9068.
10. Teulle, A.; Marty, R.; Viarbitskaya, S.; Arbouet, A.; Dujardin, E.; Girard, C.; des Francs, G. C., Scanning Optical Microscopy Modeling in Nanoplasmonics. *J. Opt. Soc. Am. B-Opt. Phys.* **2012**, *29* (9), 2431-2437.